Dilution of reactive plumes: evolution of concentration statistics under diffusion and nonlinear reaction

Tomás Aquino, Camille Bouchez, Tanguy Le Borgne

Dilution of reactive plumes: evolution of concentration statistics under diffusion and nonlinear reaction

Tomás Aquino[1,*], Camille Bouchez[1], and Tanguy Le Borgne[1]

[1]*Univ. Rennes, CNRS, Géosciences Rennes, UMR 6118, 35000 Rennes, France*
*Corresponding author: tomas.decamposaquino@univ-rennes1.fr

Abstract

Concentration fields of solutes in porous media often exhibit large fluctuations, driven by physical and chemical heterogeneity from the pore to the Darcy scale. For many applications, ranging from reactive transport modeling to toxicology, the knowledge of mean concentrations is not sufficient, and quantifying concentration variability is necessary. The probability density function (PDF) of concentration quantifies the frequency of occurrence of concentration values throughout a spatial domain. While evolution equations and analytical solutions for the concentration PDF exist for conservative solutes, less is known about its evolution under the joint action of transport and reaction. In this work, we investigate how dilution of a reactive plume by diffusion affects the statistics of concentrations. While mixing has no effect on first-order reactions, its coupling with nonlinear reactions leads to non-trivial effective kinetics relevant for a broad range of reactive transport problems. We study the evolution of the concentration PDF under diffusion and nonlinear reaction in one spatial dimension, which represents a critical step towards further coupling with heterogeneous advection. We show that the dependence of the scalar dissipation rate on concentration encodes the impact of diffusive transport on the concentration PDF and derive a dynamical equation for its time evolution. Using a weak-coupling approximation for the reaction and diffusion dynamics, we derive analytical predictions for the concentration PDF and its moments. Our results provide new insights into how diffusion and reaction control concentration variability and open new opportunities for coupling mixing models with chemical reactions.

Highlights

- We introduce a general framework quantifying the link between concentration PDFs and spatial concentration profiles.

- We derive a dynamical equation for the evolution of the concentration PDF under diffusion and nonlinear reaction in 1D.

- We derive analytical predictions for the concentration PDF and its moments using a weak-coupling approximation.

1 Introduction

Quantifying the variability in solute concentrations in the subsurface is of primary importance to a large range of applications, including reactive transport modeling (e.g., [1]), characterizing the natural chemical signature of groundwater systems (e.g., [2]), and assessing human health risks associated with contaminant transport (e.g., [3]). In particular, when reaction rates depend nonlinearly on available concentrations, effective reaction rates can differ by orders of magnitude from reaction rates determined under well-mixed conditions [4–7]. In such cases, knowledge of mean concentrations is not sufficient

to predict overall reaction rates, which requires additional knowledge about the spatial variability of concentration values and local reaction rates.

Concentration probability density function (PDF) methods aim to quantify transport and reaction processes in terms of the spatial statistics (i.e., frequency of occurrence of given values) of transported scalars [8–11]. These methods were originally developed in the context of turbulent flows, where they have been extensively employed to model both conservative transport [12–17] and reactive transport with an emphasis on combustion [18–23]. More recently, these methods have gained popularity in the context of porous media to study conservative [2, 24–33] and reactive [34–40] mixing. The statistics of concentrations have been studied in relation to different types of fluctuations. The first approach is to study concentration fluctuations with respect to an average transport model, such as the advection–dispersion equation [24–26], in terms of a stochastic transport model such as the continuous time random walk [28, 41]. Regarding, for instance, average concentrations at a given spatial position, fluctuations typically arise from variability in particle transit times due to heterogeneity. A second approach is to characterize uncertainty in concentrations due to uncertainty in model parameters, such as flow velocities and reaction rates [29, 42–45]. These methods quantify the variability in concentrations due to uncertainty in physical and chemical parameters. A third point of view is to consider the variability in concentrations over the spatial extension of a solute plume which arises from known transport and reaction processes. Even with homogeneous physical and chemical parameters, mean concentrations and associated fluctuations evolve under the combined effect of transport and reaction. In this context, the concentration PDF provides a useful tool to quantify the spatial frequency of occurrence of different solute concentration values, and to provide information about the mixing state of solute plumes without explicitly resolving the corresponding spatial profiles [31].

Here, we follow this last approach to study how the dilution of a reactive plume by diffusive mixing affects concentration statistics (Fig. 1). In this context, evolution equations have been derived for the conservative concentration PDF by quantifying the formation and interactions of lamellar structures in concentration fields subject to advection and diffusion [30, 31, 46]. Recent developments have extended these theories to mixing-limited bimolecular reactions [47]. Here, we consider a different reactive transport problem in which mixing does not act to bring segregated reactants into contact but rather to dilute a reactive plume. This system is relevant to a broad range of reactive transport problems [6, 7], including situations where transported solute plumes react nonlinearly with a solid phase as they get diluted by mixing. This leads to new dynamics that fundamentally differ from what is known regarding mixing-limited reactions across diffusing or dispersing fronts [48–51].

We investigate the coupling of dilution by diffusive mixing with the nonlinear degradation of a single species locally undergoing diffusion in one spatial dimensional and decaying at a rate proportional to an arbitrary power of concentration (Fig. 1). We generalize the results of [7] for the evolution of total mass and mean concentration to the evolution of the full concentration PDF, and we obtain a dynamical equation for the latter in terms of the scalar dissipation rate [52–56], expressed as a function of concentration. In addition to the mean concentration, the concentration PDF formulation allows us to quantify higher-order concentration moments, such as the concentration variance, which provides information about the variability in concentration values observed throughout a spatial domain. Building on the weak-coupling approximation developed in [7], we relate the evolution of the concentration PDF and its moments to the evolution of the maximum concentration, and quantify the resulting anomalous kinetics.

In the interest of developing and illustrating the new method proposed here, the class of reaction–diffusion problems we analyze introduces significant simplifications. In particular, we consider a one-dimensional problem and neglect heterogeneous advection effects. In addition, the weak-coupling approach involves a Gaussian approximation for the solute plumes at late times. Although reaction under diffusion or dispersion in the absence of advective heterogeneity has been studied in its own right in the context of porous media [4, 57–61], these conditions may be seen as fundamental building blocks in the theory of mixing in heterogeneous flows. In the presence of heterogeneous flow fields characteristic of porous media, solute plumes are deformed into a collection of elongated structures termed lamellae (Fig. 1) [31]. Using the Ranz transform [62], the resulting compression–diffusion–reaction equation can be mapped onto a one-dimensional diffusion–reaction equation, which motivates
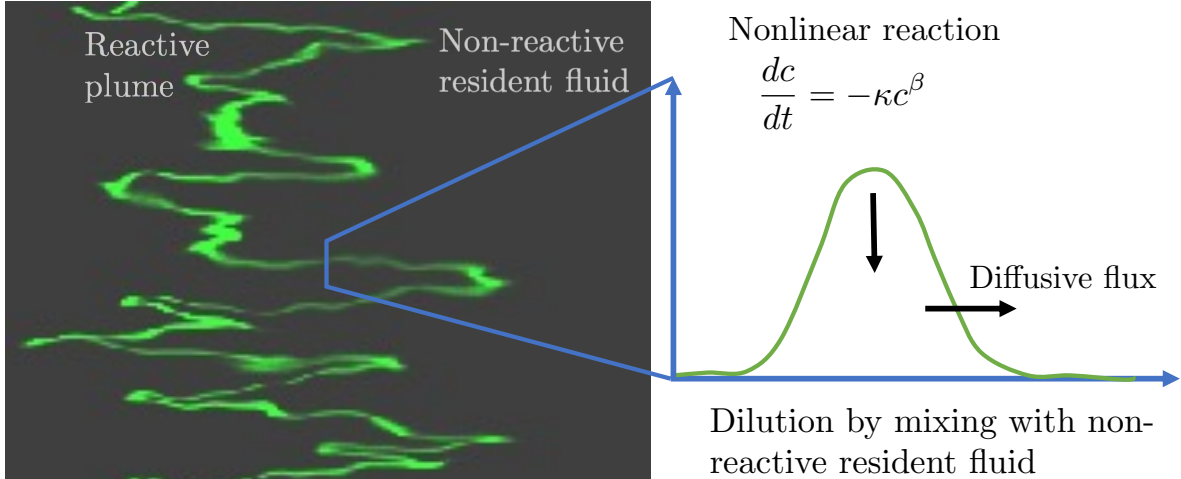
Figure 1: Illustration of the reactive transport problem under consideration (adapted from a simulation of transport at the Darcy scale in a heterogeneous permeability field [30]). We consider a plume of reactive solute (green) that undergoes nonlinear decay either by reaction with the solid, with another solute in excess everywhere, or with another solute that is well mixed inside the plume. The plume is diluted by mixing with the non-reactive resident fluid (black) while it reacts, leading to non-trivial effective reaction rates [7]. The latter are governed by the coupling of nonlinear reaction with the diffusive flux along concentration gradients. Here, we study the one-dimensional diffusion–reaction problem, which represents the first step towards solving the full advection–diffusion–reaction system.

the present study.

The paper is structured as follows. Section 2 introduces a general definition for the concentration PDF associated with a given spatial profile and explores its key properties. In Section 3, in light of these concepts, we derive a governing equation for the dynamics of the concentration PDF of a solute undergoing diffusion-induced dilution in one spatial dimension and nonlinear reaction described locally by a power-law decay of concentration. In this context, we also discuss the relationship between this simplified one-dimensional problem and reaction–diffusion in the presence of heterogeneous flows typically found in porous media, based on the Ranz transform. We then study the one-dimensional problem and the associated effective kinetics in terms of the weak-coupling approximation in Section 4. Conclusions and an overall discussion of the results are presented in Section 5. Some additional technical derivations are provided in the Appendices.

2   The concentration PDF

This section is concerned with providing a general definition of the concentration PDF associated with arbitrary spatial concentration profiles. We first present the general multispecies formulation, and then discuss the single-species case. We provide a detailed discussion of the properties of the concentration PDF, as well as of its numerical computation. The approach developed here, which forms the basis for the subsequent sections, builds on that introduced in [63] regarding Eulerian velocity PDFs. The main concepts behind the concentration PDF, which quantifies the spatial frequency of occurrence of different concentration values, are illustrated in Fig. 2 for a one-dimensional, single-species concentration profile.

Before proceeding, we introduce some notation that will be employed throughout. The concentration $\underline{C}(\boldsymbol{x};t)$ at a given location $\boldsymbol{x}$ and time t, with $\underline{C} = (C_1, \ldots, C_{n_s})$, is defined so that $\underline{C}(\boldsymbol{x};t)\,d\boldsymbol{x}$ is the mass in an infinitesimal volume $d\boldsymbol{x}$ centered at $\boldsymbol{x} = (x_1, \ldots, x_d)$ of each chemical species $1, \ldots, n_s$. We use an underscore to denote quantities whose components relate to concentration species (of which there are a number n_s), and boldface to denote spatial vectors (which have components according to
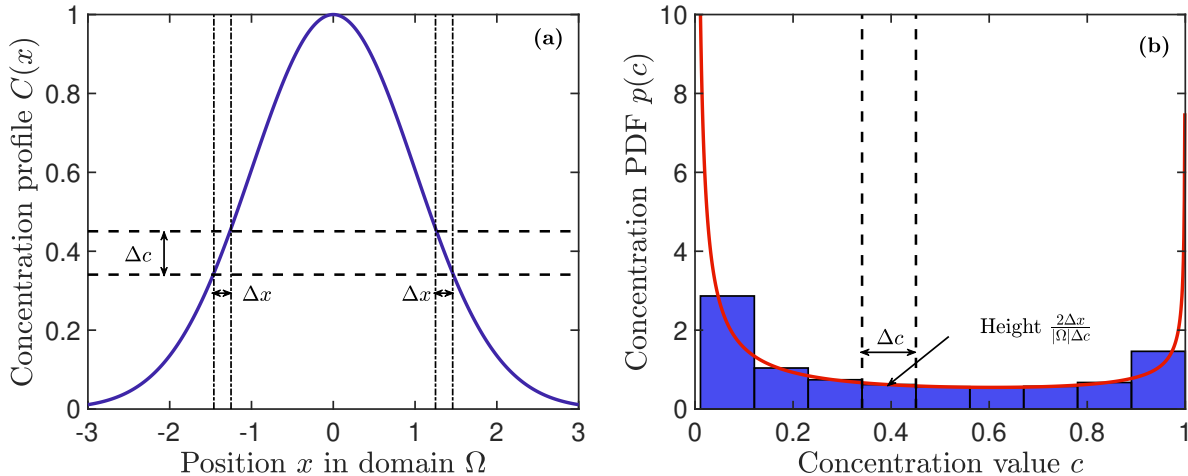
Figure 2: Illustration of the key concepts underlying the concentration PDF. **(a):** Example spatial concentration profile, a Gaussian with unit variance and unit height, restricted to the spatial domain $\Omega = [-3, 3]$ of size $|\Omega| = 6$. **(b):** Corresponding concentration PDF. Given a spatial profile, the concentration PDF quantifies the spatial frequency of occurrence of different concentration values $c = C(x)$ occurring at some position(s) x. When concentration values are discretized into bins of width Δc, the PDF value $p(c)$ is approximated by the fraction of the domain of the domain where the concentration c falls in this range, divided by Δc to obtain a probability density (bars in panel b). The continuous PDF (solid line in panel b) is obtained in the limit of infinitesimal bin widths dc. Each infinitesimal region dx around a point where $C(x) = c$ contributes a probability density $(dx/dc)/|\Omega| = 1/(|\Omega||dC(x)/dx|)$. This causes a divergence of the PDF at the maximum concentration $c_M = 1$, where the gradient is zero, and contributes to a large value at the minimum concentration $c_m = C(3) = C(-3)$, where the gradient is small. These concepts are quantified and explored in detail throughout the text.

the spatial dimension d). We denote by $|A|$ the d-volume of a spatial domain A (volume for $d = 3$-dimensional A, area for $d = 2$, length for $d = 1$, and number of points for $d = 0$). As usual, $|\boldsymbol{a}|$ for a vector $\boldsymbol{a}$ denotes its Euclidean norm. We consider a spatial domain $\Omega(t)$ where the concentrations are defined for each time t, and denote by $\boldsymbol{X}(t)$ a random variable with a uniform distribution over $\Omega(t)$. The average with respect to $\boldsymbol{X}(t)$, i.e., the spatial average, is denoted by $\overline{\cdot}$. We also introduce, for each time t, a random variable $\underline{C}(t)$ taking concentration values according to their spatial probability of occurrence, and denote the average with respect to it (i.e., over concentrations) by $\langle \cdot \rangle$. As will be discussed in more detail below, the two averages, while conceptually different, yield equivalent results. That is, for an arbitrary function $f(\underline{c}, t)$ of concentrations $\underline{c}$ and times t,

$$\overline{f(\underline{C}[\boldsymbol{X}(t), t])} = \frac{1}{|\Omega(t)|} \int_{\Omega(t)} d\boldsymbol{x} \, f(\underline{C}[\boldsymbol{X}(t), t]) = \int_0^\infty d\underline{c} \, f(\underline{c}, t) p(\underline{c}; t) = \langle f[\underline{C}(t), t] \rangle, \tag{1}$$

where, at each time t, $p(\cdot; t)$ is the concentration PDF, to be formally defined momentarily.

2.1 General formulation for a multispecies system

At each time t, the concentration PDF $p(\cdot; t)$ is defined so that $p(\underline{c}; t) \, d\underline{c}$ is the probability, in the sense of spatial frequency of occurrence, of finding a concentration in the infinitesimal vicinity $d\underline{c} = \prod_{j=1}^{n_s} dc_j$ of $\underline{c}$ in the domain $\Omega(t)$. According to this definition, we have

$$p(\underline{c}; t) = \overline{\delta[\underline{c} - \underline{C}[\boldsymbol{X}(t); t]]} = \frac{1}{|\Omega(t)|} \int_{\Omega(t)} d\boldsymbol{x} \, \delta[\underline{c} - \underline{C}(\boldsymbol{x}; t)], \tag{2}$$

4

where $\delta(\cdot)$ is the Dirac delta. Intuitively, this expression encodes the fact that the contributions to the probability of having a value $\underline{c}$ of concentration at time t correspond to points $\boldsymbol{x}$ where $\underline{C}(\boldsymbol{x};t) = \underline{c}$, which are "counted" by the Dirac delta in accordance with the continuous nature of concentrations (for the general theory of PDFs as averages of Dirac deltas, see, e.g., [64]). This corresponds to the continuum limit described in Fig. 2.

The concentration PDF contains information about the full structure of point statistical variability of concentrations. According to the definition, Eq. (2), moments of concentration, such as the component-wise mean concentrations $\langle \underline{C}(t) \rangle$ and variances $\underline{\sigma_c}^2 = \langle \underline{C}^2(t) \rangle - \langle \underline{C}(t) \rangle^2$ (representing not a spatial variance but variability with respect to the mean concentration), may be computed given knowledge of the PDF, and agree with those obtained from the spatial profile. In particular,

$$\langle \underline{C}(t) \rangle = \int\limits_0^\infty d\underline{c}\,\underline{c}\,p(\underline{c};t) = \frac{\underline{M}(t)}{|\Omega(t)|} = \overline{\underline{C}[\boldsymbol{X}(t);t]}, \tag{3}$$

where the total component masses are given by

$$\underline{M}(t) = \int\limits_{\Omega(t)} d\boldsymbol{x}\,\underline{C}(\boldsymbol{x};t). \tag{4}$$

It is important to note that $\Omega(t)$ may be time-dependent, but its size $|\Omega(t)|$ must be finite at all times, because a uniformly-distributed random variable $\boldsymbol{X}(t)$ does not exist in an infinite domain. Intuitively, this is related to the fact that the concentration PDF is defined in terms of the spatial frequency of occurrence of concentration values. Thus, if the total component masses are finite, most regions in an infinite domain $\Omega(t)$ must have a vanishing concentration, and $p(\underline{c};t) = 0$ for all $\underline{c} \neq 0$, so that we must have trivially $p(\underline{c};t) = \delta(\underline{c})$ by normalization. In practice, as will be discussed in more detail below, this means that in order to define a non-trivial concentration PDF we must consider either a finite, fixed reference domain Ω, or a minimum concentration threshold c_m such that $\Omega(t)$ is the region where concentrations are above this threshold. Finally, we note that, in an infinite periodic system, the concentration PDF may be naturally defined over a single period. The previous argument can be circumvented in this case because the total mass in such an infinite system is infinite, although the mass per period is finite.

2.2 Single-species formulation

Writing the concentration PDF in a more useful analytical form requires changing variables in the Dirac delta in Eq. (2), in order to identify the spatial points $\boldsymbol{x}$ that contribute to the integral for a given value of concentration $\underline{c}$. In other words, we must invert the relations $\underline{C}(\boldsymbol{x};t) = \underline{c}$, which form a set of n_s constraints in d dimensions. These constraints are not necessarily independent, and this is a difficult problem in general from an analytical perspective. We now derive a simple analytical form for the single-species case. We write $C = C_1$ and $c = c_1$ for the single species component. A numerical computation procedure, also valid for the general multispecies PDF, is discussed in Appendix A.

Assuming $C(\cdot;t)$ to be smooth, the Dirac delta can be expressed as a simple-layer integral [65],

$$\delta[c - C(\boldsymbol{x};t)] = \int\limits_{\Lambda(c;t)} dS(\boldsymbol{y})\,\frac{\delta(\boldsymbol{x} - \boldsymbol{y})}{|\nabla C(\boldsymbol{y};t)|}, \tag{5}$$

where $dS(\boldsymbol{x})$ is the $(d-1)$-area element at point $\boldsymbol{x}$ on the $(d-1)$-surface consisting of the points in the domain at time t at which the concentration has value c, and which do not constitute a local extremum (or zero-gradient inflection point). Formally, this surface is defined as $\Lambda(c;t) = \{\boldsymbol{x} \in \Omega(t) \mid C(\boldsymbol{x};t) = c \wedge |\nabla C(\boldsymbol{x};t)| \neq 0\}$. Note that, for the one-dimensional example in Fig. 2, $\Lambda(c) = 2$ for all concentrations strictly between the minimum and maximum values. This is discussed in more detail

in Section 2.4. Substituting Eq. (5) in Eq. (2), we find

$$p(c;t) = \int\limits_{\Lambda(c;t)} \frac{dS(\boldsymbol{x})}{|\Omega(t)||\nabla C(\boldsymbol{x};t)|}. \tag{6}$$

This form corresponds to the intuitive notion of a change of variables mentioned above: it expresses the contribution to the probability density of a given value c of concentration as a spatial integral over the spatial region where the concentration takes the required value (see also Fig. 2). This spatial region has dimensionality one less than the full space due to the constraint $C(\boldsymbol{x};t) = c$. This result holds for smooth, non-constant $C(\cdot;t)$. The contributions of concentrations found near spatial concentration extrema and in extended regions of constant concentration are discussed below.

Equation (6) can also be expressed so as to highlight the role of concentration gradients associated with a given concentration in determining the value of the PDF. To this end, consider the harmonic average $g_h(c;t)$ of the concentration gradient magnitudes in $\Lambda(c;t)$. By definition, it is given by

$$g_h(c;t) = \left[\frac{1}{|\Lambda(c;t)|} \int\limits_{\Lambda(c;t)} \frac{dS(\boldsymbol{x})}{|\nabla C(\boldsymbol{x};t)|} \right]^{-1}. \tag{7}$$

Substituting this definition in Eq. (6) immediately yields the simple form

$$p(c;t) = \frac{|\Lambda(c;t)|}{|\Omega(t)|g_h(c;t)}. \tag{8}$$

The proportionality to the inverse of a concentration gradient magnitude is a consequence of the fact that $p(c;t)$ is a density, i.e., a probability per unit concentration. Spatial regions where the concentration gradient is low correspond to a higher density around the corresponding concentration value due to the slow variation. To understand this, consider a surface $\Lambda(c;t)$ over which the gradient magnitude $g_h(c;t) = |\nabla C|$ is homogeneous and therefore equal to its harmonic average. A small variation dc of concentration occurs over a distance $dz = dc/g_h(c;t)$ along the concentration gradient. The gradient is locally perpendicular to the surface of constant concentration, so that the spatial volume associated with an occurrence of concentration in $[c, c + dc]$ is $|\Lambda(c;t)|dz$. Correspondingly, the contribution to the probability $p(c;t)\,dc$ of concentration in this range is $|\Lambda(c;t)|\,dz/|\Omega(t)|$. Thus, its contribution to the concentration PDF $p(c;t)$ is $|\Lambda(c;t)|/[|\Omega(t)|g_h(c;t)]$, in agreement with Eq. (8). This is illustrated for a one-dimensional profile in Fig. 2. More generally, if the gradient is not constant over the surface, the same argument can be applied locally, using the area element dS introduced above and the volume element $dSdz$. The inverse proportionality to the harmonic average then arises due to the inverse proportionality of the local contributions to the inverse gradient magnitude, which must be integrated over. This provides an intuitive explanation for Eq. (6) and recovers Eq. (8).

2.3 Extrema and constant-concentration regions

We now study the impact on the concentration PDF of local extrema of the spatial concentration profile, at which $|\nabla C(\boldsymbol{x};t)| = 0$. Near an extremum c_0 at position $\boldsymbol{x}_0$ and time t, we have $C(\boldsymbol{x}_0 + \Delta\boldsymbol{x};t) \approx c_0 + \Delta\boldsymbol{x} \cdot H(\boldsymbol{x}_0;t)\Delta\boldsymbol{x}/2$ and $\nabla C(\boldsymbol{x};t) \approx H(\boldsymbol{x}_0;t)\Delta\boldsymbol{x}$, where $H(\boldsymbol{x}_0;t)$ is the Hessian matrix of concentration at position $\boldsymbol{x}_0$ and time t, with components $H_{ij}(\boldsymbol{x}_0;t) = \nabla_i\nabla_j C(\boldsymbol{x};t)|_{\boldsymbol{x}=\boldsymbol{x}_0}$. We find that in $d = 1$ the PDF of concentration behaves in a vicinity Δc of c_0 as

$$p(c_0 + \Delta c;t) \approx \left(|\Omega(t)|\sqrt{\Delta c \frac{\partial^2 C(x;t)}{\partial x^2}\Big|_{x=x_0}} \right)^{-1}, \tag{9}$$

to first order in $|\Delta c| \ll c_0$, for $\Delta c < 0$ near a maximum and $\Delta c > 0$ near a minimum. This type of divergent behavior due to a spatial maximum can be observed in Fig. 2. We note that this is an

integrable divergence, that is, the integral of $p(\cdot; t)$ converges near c_0 as necessary for a PDF. This result is a direct consequence of the fact that for a smooth function near an extremum the behavior of the function is quadratic, and the behavior of its derivative is linear. We have assumed the extremum is non-degenerate, so that the second derivative is nonzero; otherwise, higher order terms are important and the behavior is different.

In arbitrary dimension, we provide an argument based on dimensional analysis. First, note that the qualitative behavior near an extremum is determined by the Hessian determinant $|H|$ and the distance $|\Delta \boldsymbol{x}|$ to the maximum; thus, the gradient near an extremum obeys $|\nabla C| \propto |H|^{1/d}|\Delta \boldsymbol{x}|$, and the concentration changes as $|\Delta c| \propto |\nabla c||\Delta \boldsymbol{x}| \propto |H|^{1/d}\Delta x^2$. The second equation gives $|\Delta \boldsymbol{x}| \propto |H|^{-1/(2d)}|\Delta c|^{1/2}$, and substituting in the first leads to $p(c_0 + \Delta c; t) \approx |\Lambda(c_0 + \Delta c; t)|/[|\Omega(t)||\nabla C|] \propto |\Lambda(c_0 + \Delta c; t)|/[|\Omega(t)||H|^{1/(2d)}|\Delta c|^{1/2}]$. Substituting $|\Lambda(c_0 + \Delta c; t)| \propto |\Delta \boldsymbol{x}|^{d-1}$ for the $(d-1)$-area of the surface of concentration $c_0 + \Delta c$ yields

$$p(c_0 + \Delta c; t) \propto \frac{|\Delta c|^{d/2-1}}{|\Omega(t)||H|^{1/2}}. \tag{10}$$

Thus, there is no divergence in $d \geqslant 2$. In $d = 2$, extrema of the spatial concentration correspond to extrema of the concentration PDF, and in $d = 3$ they correspond to zeros. As before, we have assumed that the minimum is non-degenerate, i.e., $|H| \neq 0$. As a simple example of degeneracy, consider a concentration field which is constant along the second and third dimensions, and exhibits a regular extremum along the first dimension. As expected, the divergence as the extremum is neared then depends only on the distance Δx along the first dimension, and the square-root divergence of the concentration PDF characteristic of $d = 1$ is recovered.

If $C(\cdot; t)$ is constant in space (i.e., the concentration is homogeneous), or if we relax the smoothness assumption so that $|\nabla C(\cdot; t)|$ may be zero in open sets by letting $C(\cdot; t)$ be non-differentiable at their boundary (i.e, piecewise-smooth), these sets may contribute additional terms to the concentration PDF. Consider first that the concentration is piecewise-constant. Each set $\Omega_i(t)$ where the concentration takes a given position-independent value $c_i(t)$ at time t is associated with a probability $|\Omega_i(t)|/|\Omega(t)|$. Note that there must be a finite number $N(t)$ of such constant-concentration sets at each time, and thus a finite number of corresponding concentration values, because open sets have nonzero measure and sets corresponding to different concentrations are disjoint, so that $|\Omega(t)| = \sum_{i=1}^{N(t)} |\Omega_i(t)|$. Therefore,

$$p(c; t) = \sum_{i=1}^{N(t)} \frac{|\Omega_i(t)|}{|\Omega(t)|} \delta[c - c_i(t)]. \tag{11}$$

The Dirac deltas express the fact that concentration takes a single specific value within spatially-homogeneous regions. If the concentration is piecewise-smooth and non-constant over certain parts of the domain, Eq. (8) may be applied separately to each such region, and the contributions of all constant and non-constant regions summed over to obtain the full concentration PDF.

2.4   One-dimensional Gaussian profile

As a relevant example which will play a central role in Section 3, we consider a single-species Gaussian concentration profile in $d = 1$ spatial dimension (Fig. 1), characterized by spatial variance $\sigma^2(t)$ and total mass $M(t)$:

$$C(x; t) = \frac{M(t)}{\sqrt{2\pi\sigma^2(t)}} \exp\left[-\frac{x^2}{2\sigma^2(t)}\right]. \tag{12}$$

The corresponding regions of constant concentration c are zero-dimensional, $\Lambda(c; t) = \{x | x = \pm x_c(c; t)\}$. Inverting $C(x; t) = c$ for x,

$$x_c(c; t) = \sqrt{2\sigma^2(t)\ln[c_M(t)/c]}, \tag{13}$$

where

$$c_M(t) = \frac{M(t)}{\sqrt{2\pi\sigma^2(t)}} \tag{14}$$

7

is the maximum concentration at time t. The zero-dimensional area element on $\Lambda(c;t)$ is a sum of point measures concentrated at the two points $\pm x_c(c;t)$ where the concentration takes a given value, $dS(x) = (\delta[x + x_c(c;t)] + \delta[x - x_c(c;t)])\,dx$. For all $c < c_M(t)$, $|\Lambda(c;t)| = 2$ because it consists of two points. The gradient of concentration magnitudes at $\pm x_c(c;t)$ have the same value, so that their harmonic average is equal to this value and given by

$$g_h(c;t) = |\nabla C(x;t)|_{x=\pm x_c(c;t)} = \sqrt{\frac{2c^2 \ln[c_M(t)/c]}{\sigma^2(t)}}. \tag{15}$$

As discussed in Section 2, we must consider a finite domain in order for the concentration PDF to be well-defined. This can be conveniently achieved through one of two possible approaches. The first considers a fixed (i.e., time-independent) reference domain Ω centered at $x = 0$. In this case, a time-dependent minimum concentration $c_m(t) = c_M(t) \exp\{-|\Omega|^2/[8\sigma^2(t)]\}$ is found at the fixed domain boundaries. Alternatively, we fix a (time-independent) minimum concentration c_m, and consider $\Omega(t) = \{x | C(x;t) > c_m\}$, the time-dependent spatial domain where concentration are above the minimum value. In this case, c_m can be thought of as a lower detection limit, and the concentration PDF as being computed over the region of space where non-zero concentration is detected. In either case, using Eq. (8) leads to the concentration PDF

$$p(c;t) = \frac{H[c_M(t) - c]H[c - c_m(t)]}{2c\sqrt{\ln[c_M(t)/c]\ln[c_M(t)/c_m(t)]}}, \tag{16}$$

where under the second approach $c_m(t) = c_m$ is constant. This PDF is illustrated in Fig. 2, and it agrees with the result reported, e.g., in [30]. By noting that $|\Omega(t)| = 2x_c[c_m(t);t]$ and using Eqs. (13) and (14), we find

$$|\Omega(t)| = \frac{2M(t)}{c_M(t)} \sqrt{\frac{\ln[c_M(t)/c_m(t)]}{\pi}}, \tag{17}$$

and the concentration PDF can thus also be expressed as

$$p(c;t) = \frac{M(t)H[c_M(t) - c]H[c - c_m(t)]}{|\Omega(t)|cc_M(t)\sqrt{\pi \ln[c_M(t)/c]}}. \tag{18}$$

Note that, for fixed t, setting $c = c_M(t) - \Delta c$ and expanding to first order in Δc recovers the expected $\Delta c^{-1/2}$ divergence due to the presence of a spatial maximum discussed in Section 2.3. For small concentrations compared to the peak value, this PDF scales as $1/c$ with logarithmic corrections.

Using these results and Eq. (12), it can be verified by direct computation that the mean concentration is given by

$$\langle C(t) \rangle = \overline{C(X;t)} \approx \frac{M(t)}{|\Omega(t)|} = \frac{c_M(t)}{2} \sqrt{\frac{\pi}{\ln[c_M(t)/c_m(t)]}}, \tag{19}$$

and for the second moment of concentration we have

$$\langle C^2(t) \rangle = \overline{C^2(X;t)} \approx \frac{M(t)c_M(t)}{\sqrt{2}|\Omega(t)|} = \frac{c_M^2(t)}{2} \sqrt{\frac{\pi}{2\ln[c_M(t)/c_m(t)]}}, \tag{20}$$

where the approximation corresponds to approximating the total mass $M(t)$ in the infinite domain by the mass within $\Omega(t)$, over which concentration is larger than $c_m(t)$. Note that, in particular, this approximation requires $c_M(t) \gg c_m(t)$, that is, the lower detection limit must be small compared to the peak concentration. Under the same approximation, the variance of concentration is thus

$$\sigma_c^2(t) \approx \frac{\pi c_M^2(t)}{4\ln[c_M(t)/c_m(t)]} \left[\sqrt{\frac{2\ln[c_M(t)/c_m(t)]}{\pi}} - 1 \right], \tag{21}$$

or equivalently

$$\frac{\sigma_c^2(t)}{\langle C(t) \rangle^2} \approx \sqrt{\frac{2\ln[c_M(t)/c_m(t)]}{\pi}} - 1. \tag{22}$$

8

Note that the mean and variance of concentration represent the mean value and the associated variability in the frequency of occurrence of concentration values found throughout the domain. They differ from the more common metrics of mean plume position, which here is zero, and spatial or plume variance, which here is $\sigma^2(t)$.

3 Concentration PDF evolution under nonlinear reaction and diffusion

In this section, we apply the concepts developed above to the single-species, one-dimensional reaction–diffusion problem

$$\frac{\partial C(x;t)}{\partial t} = D\frac{\partial^2 C(x;t)}{\partial x^2} - r[C(x;t)], \tag{23}$$

where the reaction rate as a function of concentration has the form

$$r(c) = \kappa c^\beta, \tag{24}$$

with $\beta > 0$ the order of the reaction and κ the reaction rate constant in units of $[C^{1-\beta}T^{-1}]$. Understanding the role and dynamics of concentration statistics under one-dimensional reaction–diffusion represents a fundamental first step towards treating more complex reaction problems in heterogeneous flow fields. In this connection, we discuss the Ranz transform, which was developed to quantify mixing and reaction in the context of turbulence and combustion problems [62, 66] and has more recently been employed to study these phenomena in porous media [30, 67, 68]. The goal of the Ranz transform is to exploit the fact that material elements in an incompressible flow tend to orient themselves according to the principal directions of strain-induced stretching (Fig. 1), forming thin lamellar structures (lines in 2D or sheets in 3D) [48, 69–74, 74–76].

Due to incompressibility, the thickness of such a material element along the principal axis of compression is given by $s(t) = s(0)A(0)/A(t)$, where $A(t)$ is its area (or length in 2D). Assuming that local compression is well described by a first-order Taylor expansion of the flow, and neglecting concentration gradients on the surface in comparison to normal gradients along the compression direction ζ, the advection–diffusion–reaction equation becomes [30, 67, 74, 75]

$$\frac{\partial C}{\partial t} = -\frac{\zeta}{s}\frac{ds}{dt}\frac{\partial C}{\partial \zeta} + D\frac{\partial^2 C}{\partial \zeta^2} - r(C). \tag{25}$$

These approximations provide a very good description of transport at high Péclet number [30, 74, 75]. Applying the Ranz transform [62],

$$\tau = \int_0^t dt' \frac{s^2(0)}{s^2(t')}, \qquad\qquad \xi = \frac{s(0)}{s(t)}\zeta, \tag{26}$$

reduces Eq. (25) to a diffusion–reaction equation in the new time τ and rescaled transverse coordinate ξ, which takes into account the history of advective deformation:

$$\frac{\partial C}{\partial t} = D\frac{\partial^2 C}{\partial \xi^2} - \frac{s^2}{s_0^2}r(C). \tag{27}$$

Thus, the full advection–diffusion–reaction problem reduces to a collection of one-dimensional diffusion–reaction problems over lamellae. Solving this problem remains highly nontrivial, as it requires determining the statistics of thicknesses $s(t)$ and those of lamella coalescence (overlapping) [30, 46, 67, 68, 77, 78], and the solution of the one-dimensional reaction–diffusion problem (27) for given $s(\tau)$, where the reaction rate becomes time-dependent according to a rescaling by $s^2(\tau)/s_0^2$. Treating the full problem is beyond the scope of this work. Here, we restrict ourselves to the purely-diffusive case, Eq. (23), which corresponds to setting $s^2/s_0 = 1$ in Eq. (27), with the power-law reaction rate (24).

The dynamics remain nontrivial even under this simplified scenario. When the reaction is nonlinear (order β nonzero and different from unity), the effective kinetics, representing the overall reaction rate for a given amount of available mass, depend on the spatial variability of concentration. In other words, the global reaction rate $dM(t)/dt$ for the total mass is not given by $\kappa M^\beta(t)$, except when $\beta = 1$ or when the system is well mixed, i.e., uniformly characterized by a single concentration value. Similar considerations apply to the reaction rate in terms of the mean concentration instead of the total mass. Nonetheless, knowledge of the point statistics of concentration as encoded in the concentration PDF is sufficient to fully characterize the global reaction rate, which can be obtained by integrating Eq. (23) over the domain $\Omega(t)$. Using integration by parts, the diffusive term can be seen to contribute $2D|\partial C/\partial x|$ evaluated at the domain boundaries, which we neglect under the assumption of a small lower detection limit c_m as above, we obtain

$$\frac{dM(t)}{dt} = - \int\limits_0^\infty dc\, r(c)p(c;t) = -\kappa \int\limits_0^\infty dc\, c^\beta p(c;t),$$ (28)

where in the last equality we have expressed the integral of the reactive contribution in terms of the concentration PDF using its definition, Eq. (2).

In what follows, we will first derive a dynamical equation for the evolution of the concentration PDF, in terms of a concentration-dependent scalar dissipation rate. We will then discuss and employ the Gaussian spatial profile arising from the weak-coupling approximation of [7] to directly compute the evolution of the concentration PDF using the results of Section 2.4, and compare it to the PDF obtained from numerical solutions of Eq. (23).

3.1 Dynamical equation for the concentration PDF

The concentration PDF evolves under the combined action of transport and reaction processes. The structure of the reaction–diffusion equation (23), where transport and reaction terms locally contribute independently to the evolution of the concentration field, ensures that the same holds for the evolution of the concentration PDF for each value of concentration. We thus seek to express its evolution as

$$\frac{\partial p(c;t)}{\partial t} = \Delta p_D(c;t) + \Delta p_R(c;t),$$ (29)

where the two contributions respectively represent the effect of diffusion and reaction. Note that, while this independence holds locally, the global reaction dynamics (i.e., the evolution of the total mass and other global quantities such as the concentration mean and variance) are affected by the dynamical evolution of the plume through the combined effect of transport and reaction. These dynamics will be discussed in detail in Section 4 using a weak-coupling approximation. We focus in what follows on the case of a fixed minimum detection limit c_m and a time-varying domain $\Omega(t)$ where concentrations are above c_m. This choice avoids the introduction of an arbitrary domain devoid of physical meaning, and corresponds more closely to real-world situations, where a lower detection limit always exists. Nonetheless, note that the introduction of a fixed reference domain may be appropriate if one is in fact interested in a specific spatial region, and the formalism can be easily adapted to that case.

As shown in Appendix B, the reactive contribution in Eq. (29) is given by

$$\Delta p_R(c;t) = \frac{\partial r(c)p(c;t)}{\partial c} + p(c;t)p(c_m;t)r(c_m).$$ (30)

Note that it is completely determined given knowledge of the concentration PDF and local reaction rate as a function of concentration. The first term represents the net change in the probability density of concentration c due to reaction, and the second term guarantees the PDF remains normalized by accounting for reactive decay of concentrations below the threshold value c_m.

It should be clear that, in general, knowledge of the frequencies of occurrence of concentration values, as expressed by $p(c;t)$, is not sufficient to determine their evolution under transport. This is

10

because concentration fluxes due to advection and diffusion are sensitive to the spatial gradients in the concentration profiles. Thus, without additional information, an equation for the concentration PDF, which encodes only the point statistics of concentration, cannot be closed. However, it is possible to express the concentration PDF's evolution in terms of an additional mixing metric, which corresponds to the scalar dissipation rate (see, e.g., [53, 54]),

$$\chi_x(x;t) = (\nabla C) \cdot (D\nabla C), \tag{31}$$

expressed as a function of concentration. We make the simplifying assumption that the initial concentration profile $C(x,0)$ is symmetric about the origin and monotonically decreasing away from it (as happens, e.g., for a Gaussian profile or a square pulse). In that case, these properties hold for all times, so that a given concentration value is associated with a single concentration gradient magnitude, simplifying the description. Under these assumptions, the concentration-dependent scalar dissipation rate is given by

$$\chi(c;t) = \chi_x[\pm x_c(c;t);t] = Dg_h^2(c;t), \tag{32}$$

where the harmonic average gradient magnitude g_h is equal to the gradient magnitude at both points $\pm x_c$ where the concentration is equal to c. As shown in Appendix B, we have for the transport contribution:

$$\Delta p_D(c;t) = p(c;t) \left[\frac{1}{4} \frac{\partial \ln \chi(c;t)}{\partial c} \frac{\partial \chi(c;t)}{\partial c} - \frac{1}{2} \frac{\partial^2 \chi(c;t)}{\partial c^2} - \frac{p(c_m;t)}{2} \frac{\partial \chi(c;t)}{\partial c} \bigg|_{c=c_m} \right], \tag{33}$$

where the first and second terms arise from the impact of diffusion on the concentration gradients associated with a given concentration value, and the third term is due to the change in domain size due to concentrations dropping below c_m by diffusion.

Substituting Eqs. (30) and (33) in Eq. (29), we conclude that the combined effect of transport and reaction leads to

$$\frac{\partial p(c;t)}{\partial t} = \frac{\partial r(c)p(c;t)}{\partial c} + \left[\frac{1}{4} \frac{\partial \ln \chi(c;t)}{\partial c} \frac{\partial \chi(c;t)}{\partial c} - \frac{1}{2} \frac{\partial^2 \chi(c;t)}{\partial c^2} \right.$$
$$\left. + \left(r(c_m) - \frac{1}{2} \frac{\partial \chi(c;t)}{\partial c} \bigg|_{c=c_m} \right) p(c_m;t) \right] p(c;t). \tag{34}$$

This equation shows that the dynamical evolution of the concentration PDF for this problem is fully determined given knowledge of the local reaction rates $r(c)$ and the concentration-dependent scalar dissipation rate $\chi(c;t)$. The first (reactive) term on the right-hand side has the form of an advective contribution: the reaction rate $r(c)$ functions as an advective "velocity" (units of inverse concentration per time) generating a net flux of probability towards lower concentrations. The remaining contributions have the form of concentration-dependent sink/source terms. The first two terms in square brackets, which are governed by the scalar dissipation rate, encode the impact on the PDF of changes in concentration values and the associated gradients due to diffusive transport. The remaining terms concern the reactive and diffusive fluxes of probability towards concentration values below the detection limit. These affect the concentration PDF through the normalization across the remaining concentration values, since $\int_{c_m}^{c_M(t)} dc\, p(c;t) = 1$ by definition.

As discussed in the introduction, the scalar dissipation rate has been studied in connection with mixing in porous media. By clarifying its role in the evolution of the concentration PDF, this approach provides a promising departure point for upscaling of reaction dynamics under transport.

4 Concentration dynamics under the weak-coupling approximation

The weak-coupling approximation developed in [7] simplifies the full reaction–diffusion dynamics of Eq. (23) by assuming that, after a time on the order of the diffusion time, the concentration profile

11

379 remains Gaussian as for the conservative problem, but with a spatial variance and mass that are affected
380 by reaction. We briefly review this approach before applying the theory and concepts developed here
381 to analyze the evolution of concentration statistics.

4.1 Problem setup and nondimensionalization

383 We will focus here, as in [7], on a rectangular pulse initial condition, corresponding to constant con-
384 centration $c_0 = M_0/s_0$ over a domain $\Omega(t)$ centered at the origin and of initial width $s_0 = |\Omega(0)|$. This
385 setup correspond to a Dirac delta initial condition for the PDF, $p(c; 0) = \delta(c - c_0)$. The initial condition
386 allows for meaningful direct comparison with the well-mixed batch problem in the domain $\Omega(0)$, which
387 corresponds to the purely-reactive scenario in the absence of diffusion. In that case, $D = 0$, so that
388 the scalar dissipation rate $\chi \equiv 0$, and we denote the associated uniform solution for concentration as
389 a function of time as $c_B(t)$.

390 In addition, in order to meaningfully compare the behavior of the system across different parameter
391 values, it is convenient to nondimensionalize concentration according to the initial concentration c_0,
392 position according to the initial width s_0, and time according to the characteristic reaction time [7]
393 $\tau_R = \kappa^{-1} c_0^{1-\beta}$. Thus, denoting nondimensionalized quantities by an asterisk, nondimensional time
394 is given by t_*/τ_R, positions by $x_* = x/s_0$, and concentrations by $C_* = C/c_0$, seen as a function of
395 nondimensional times and positions. Functions of these quantities, such as the concentration PDF, are
396 nondimensionalized accordingly; further details may be found in Appendix D. In what follows, we work
397 exclusively in nondimensional units and drop the asterisks for notational brevity. The nondimensional
398 transport equation is given by

$$\frac{\partial C(x; t)}{\partial t} = \frac{1}{2 \, \mathrm{Da}} \frac{\partial^2 C(x; t)}{\partial x^2} - r[C(x, t)], \tag{35}$$

399 where we have introduced the Damköhler number

$$\mathrm{Da} = \frac{\tau_D}{\tau_R}, \qquad\qquad \tau_D = \frac{s_0^2}{2D}. \tag{36}$$

400 A large Damköhler number corresponds to fast reaction compared to the diffusion time τ_D associated
401 with the nondimensionalization lengthscale s_0, and a low Damköhler number to slow reaction. Note
402 that Eq. (34) for the evolution of the concentration PDF remains unchanged when all intervening
403 quantities are nondimensionalized.

4.2 Early times – Batch dynamics

405 Under the weak-coupling approximation, up to times on the order of the diffusion time, the concen-
406 tration distribution is approximated as not having deformed substantially with respect to the initial
407 condition, here a square pulse of unit width in nondimensional coordinates. Thus, up to nondimen-
408 sional time $t = \mathrm{Da}$, the system is taken to evolve according to reaction in a batch reactor. Since
409 variations in the spatial distribution up to this time are considered negligible and not resolved, under
410 this approximation the concentration PDF remains a Dirac delta for $t \leqslant \mathrm{Da}$, $p(c; t) \approx \delta[c - c_B(t)]$. We
411 have (see also Appendix E):

$$\frac{dc_B}{dt} = -c_B^{\beta}. \tag{37}$$

412 The special case $\beta = 1$ corresponds to linear reactions. Decay is then exponential, $c_B(t) = \exp(-t)$.
413 In this classical case, reaction and transport dynamics are fully decoupled: the exact solution of the
414 full reactive transport problem is simply the conservative transport solution, multiplied by $\exp(-t)$ to
415 account for mass loss due to reaction. For nonlinear reactions, $\beta \neq 1$, integrating Eq. (37) yields

$$c_B(t) = [1 - (1 - \beta)t]^{\frac{1}{1-\beta}} . \tag{38}$$

416 In nondimensional units, the total mass and concentration coincide for batch dynamics, because
417 the width of the pulse is approximated as constant and equal to the initial unit width in this time

⁴¹⁸ window. Thus, for $t <$ Da we approximate $M(t) \approx c_B(t)$. Note that for $\beta < 1$ the batch reaction is
⁴¹⁹ fully depleted in a finite time

$$t_f^B = \frac{1}{1-\beta}.\tag{39}$$

⁴²⁰ If $t_f^B <$ Da, the full dynamics are thus simply treated as a well-mixed batch reactor.

4.3 Late times – Gaussian profile

⁴²² For times $t <$ Da, [7] have verified that the dynamics are reasonably well approximated by a well-mixed
⁴²³ batch reactor, disregarding transport and spatial variability in concentration. We thus focus now on
⁴²⁴ times $t \geqslant$ Da, for which spatial concentration variability cannot be neglected. Starting at $t =$ Da, when
⁴²⁵ diffusion has had sufficient time to deform the concentration pulse, the weak-coupling approximation
⁴²⁶ consists in approximating the spatial profile as a Gaussian, whose properties are governed by the
⁴²⁷ combined effect of reaction and diffusion as detailed below. Consider first Eq. (34) for the dynamical
⁴²⁸ evolution of the concentration PDF. Under the Gaussian approximation, the scalar dissipation rate
⁴²⁹ can be computed analytically. From Eqs. (12) and (13) for the Gaussian profile and (77b) for the
⁴³⁰ scalar dissipation rate, we find

$$\chi(c;t) = \frac{2\pi c_M^2(t)c^2 \ln[c_M(t)/c]}{\text{Da}\, M^2(t)} H[c_M(t) - c]H[c - c_m],\tag{40}$$

⁴³¹ where we have used Eq. (14) to express the spatial variance in terms of the mass and peak concentration.
⁴³² Note that, expanding the logarithm in Taylor series for small Δc near the peak value, $c = c_M(t) - \Delta c$,
⁴³³ we find that the scalar dissipation rate approaches zero linearly with Δc. At low concentrations
⁴³⁴ compared to the peak value, it scales as c^2 with logarithmic corrections. Using Eq. (40), Eq. (34) for
⁴³⁵ the evolution of the concentration PDF becomes

$$\frac{\partial p(c;t)}{\partial t} = \frac{\partial c^\beta p(c;t)}{\partial c} + \left\{ \frac{1 + 2\ln[c_M(t)/c]}{2\ln[c_M(t)/c]} \right.$$
$$\left. + \left(1 - 2\ln\frac{c_M(t)}{c_m} + c_m^{\beta-1} \right) c_m p(c_m;t) \right\} \frac{\pi c_M^2(t)p(c;t)}{\text{Da}\, M^2(t)}.\tag{41}$$

⁴³⁶ Consider first the conservative case, corresponding to omitting the reactive terms involving c^β and
⁴³⁷ c_m^β. As explained above, we consider a Gaussian initial condition at $t =$ Da, and take the detection
⁴³⁸ limit to be sufficiently low for the mass corresponding to concentrations above c_m to be approximately
⁴³⁹ equal to the total mass for all times of interest. Then, $M(t) = 1$, and the peak concentration is given
⁴⁴⁰ by Eq. (14) with a spatial variance $\sigma^2(t) = \sigma^2(0) + (t - \text{Da})/\text{Da}$. Using Eq. (16) for the Gaussian
⁴⁴¹ concentration PDF, it can be verified by direct calculation that Eq. (34) holds identically for all c and
⁴⁴² t. As a direct verification of the combined effect of reaction and diffusion on the concentration PDF,
⁴⁴³ consider the particular case of a linear decay reaction, $r(c) = c$, for which analytical solutions are
⁴⁴⁴ available. In this case, the concentration profile remains exactly Gaussian as before, but with a total
⁴⁴⁵ mass that evolves in time as $M(t) = \exp(-t)$. The spatial variance remains unchanged with respect to
⁴⁴⁶ the conservative case, and Eq. (16) remains valid with $c_M(t)$ given by Eq. (14) as before. Once again,
⁴⁴⁷ direct computation of both sides of Eq. (41) shows that they are identical for all values of c and t.

⁴⁴⁸ Equation (41) quantifies the full evolution of the concentration PDF and sheds light on the fun-
⁴⁴⁹ damental governing processes. However, solving it directly is challenging. We will thus focus instead
⁴⁵⁰ on extending the weak-coupling approach to directly compute the concentration PDF and associated
⁴⁵¹ quantities based on the evolution of the total mass $M(t)$ and the peak concentration $c_M(t)$. This will
⁴⁵² allow us to obtain additional analytical insights into the dynamics. [7] focused on the evolution of
⁴⁵³ the total mass and spatial variance. For the purpose of determining the concentration PDF, and in
⁴⁵⁴ particular the mean concentration above a detection threshold and the associated variability, it is more
⁴⁵⁵ convenient to quantify the dynamics in terms of the evolution of total mass and peak concentration,

as the latter plays a central role (see Eqs. (12), (19), and (21)). At time $t = \text{Da}$, when we begin approximating the concentration profile as Gaussian, the mass and peak are approximated as

$$M(\text{Da}) = c_M(\text{Da}) = c_B(\text{Da}) = \left[1 - (1 - \beta)\,\text{Da}\right]^{\frac{1}{1-\beta}}, \tag{42}$$

where $c_B(\text{Da})$ is computed according to the batch solution (38). We note that in [7], instead of matching the peak value to the batch dynamics at $t = \text{Da}$, the spatial variance was set to match that of the initial square pulse, $\sigma^2(\text{Da}) = 1/12$. This leads to qualitatively similar results and makes no difference at late times. The present choice enforces continuity of $c_M(t)$ at $t = \text{Da}$, while the previous choice enforces continuity of $\sigma^2(t)$ instead. Due to Eq. (14), the approximation of a sharp transition between batch dynamics and a Gaussian profile cannot enforce the continuity of both, and for the current choice we have $\sigma^2(\text{Da}) = 1/(2\pi)$, roughly double the initial spatial variance.

The total mass dynamics are then obtained from the local reaction kinetics. That is, integrating Eq. (35) in space for fixed time and using Eq. (12) for the Gaussian profile, neglecting mass present at concentrations below the detection limit c_m, we obtain the mass evolution for $\beta > 0$ as

$$\frac{dM(t)}{dt} = -\frac{M^\beta(t)}{\sqrt{\beta}} \left[2\pi\sigma^2(t)\right]^{\frac{1-\beta}{2}}. \tag{43}$$

In order to obtain an equation for the peak concentration, we employ Eq. (35) at $x = 0$. This gives

$$\frac{dc_M(t)}{dt} = -\frac{c_M(t)}{2\,\text{Da}\,\sigma^2(t)} - c_M^\beta(t). \tag{44}$$

Using Eq. (14) to express the spatial variance in terms of the mass and peak concentration, we obtain

$$\frac{dM(t)}{dt} = -\frac{M(t)}{\sqrt{\beta}} c_M^{\beta-1}(t), \tag{45a}$$

$$\frac{dc_M(t)}{dt} = -\frac{\pi c_M^3(t)}{\text{Da}\,M^2(t)} - c_M^\beta(t). \tag{45b}$$

Note that Eq. (45a) for the overall reaction rate can also be obtained directly from the concentration PDF by using Eqs. (18) and (28). The result follows from setting $c_m = 0$ in the lower integration limit, which, for $\beta > 0$, is equivalent to neglecting the mass present at concentrations lower than c_m, as was done for the spatial profile in Eq. (43). This confirms that, as expected, knowledge of the concentration PDF directly determines overall reaction rates and mass evolution, without need for additional detailed knowledge about the spatial profile.

Equations (45), with initial conditions at time $t = \text{Da}$ according to Eq. (42), fully determine the evolution of total mass and peak concentration in this regime. Given knowledge of the mass and peak concentration, the concentration PDF for $t \geqslant \text{Da}$, based on the Gaussian assumption, is given by Eq. (16). In the examples considered here, we fix the minimum concentration, corresponding to an arbitrary lower detection limit, to $c_m = 10^{-6}$. Recall that, in nondimensional units, this refers to a detection limit six orders of magnitude below the initial concentration characterizing the rectangular pulse injection. The results are qualitatively similar for different c_m, so long as the peak concentration $c_M(t)$ remains large compared to c_m for the times of interest. If $c_M(t)$ approaches c_m, an appreciable amount of mass loss will start occurring as it drops below the detection limit. The system will then appear completely depleted, with all detectable mass and concentrations reaching zero.

In [7], good agreement was shown to hold between the total mass and spatial variance predicted by the weak-coupling approximation and numerical simulations of Eq. (35). Here, we verify the predictions of this approach, cast in terms of the total mass and peak concentration, for the full concentration PDF, as well as the time-evolution of the associated mean concentration and concentration variance. To this end, we first conduct resolved numerical simulations of the coupled diffusion and reaction problem, Eq. (35). To compute the quantities associated with model predictions, we employ Eqs. (45), which constitute ordinary rather than partial differential equations and can be efficiently solved numerically.

The numerical methods used for both these computations are detailed in Appendix C. Furthermore, we obtain analytical predictions for late-time behaviors under the weak-coupling approximation.

In order to test the applicability of the Gaussian assumption for predicting concentration variability at times $t \geqslant \mathrm{Da}$, we note that the concentration PDF associated with a Gaussian profile, Eq. (16) can be expressed in terms of concentrations rescaled by their (time-dependent) peak value, $c' = c/c_M(t)$, as

$$p'(c';t) = c_M(t)p[c_M(t)c';t] = f_p(c')\frac{H(1-c')H[c'-c'_m(t)]}{\sqrt{\ln[1/c'_m(t)]}}, \tag{46}$$

where $c'_m(t) = c_m/c_M(t)$, and

$$f_p(c') = \frac{1}{2c'\sqrt{\ln(1/c')}}. \tag{47}$$

The concentration PDF $p'(c';t)$ of rescaled concentration is independent of time except through the lower cutoff $c'_m(t)$ (on which it depends in terms of both its range and normalization). The functional dependency $f_p(c')$ on rescaled concentration under the Gaussian approximation is both time-independent and independent of the system parameters β and Da. In order to compare this to the resolved numerical results, below we compute the functional dependency according to Eq. (46), i.e., as $\sqrt{\ln[1/c'_m(t)]}c_M(t)p[c_M(t)c';t]$.

Similarly, to assess the quality of the Gaussian approximation regarding the scalar dissipation rate, we consider the rescaled form (see Eq. (40))

$$\chi'(c';t) = \frac{\mathrm{Da}\,M^2(t)}{2\pi c_M^4(t)}\chi[c_M(t)c',t] = f_\chi(c')H(1-c')H[c'-c'_m(t)], \tag{48}$$

where the functional dependency on rescaled concentration is given by

$$f_\chi(c') = c'^2\ln(1/c'). \tag{49}$$

Below, we employ Eq. (48) to compute the functional dependency from numerical simulations, similarly to the case above for the concentration PDF. Comparison of the concentration PDF functional forms provides a metric for the performance of the Gaussian approximation regarding the relative frequency of occurrence of different concentration values, and comparison of the scalar dissipation rate functional forms provides complementary information about the approximation's performance regarding the gradient values associated with each concentration value.

As they correspond to qualitatively different regimes, we consider the cases $\beta < 1$, $1 < \beta < 3$, and $\beta > 3$ separately below. In what follows, we also discuss analytical approximations for late-time behaviors. Before proceeding, we note that the starting point for these results is the fact that, for $t \geqslant \mathrm{Da}$, the concentration profile may be approximated as Gaussian with a spatial variance that increases diffusively as $\sigma^2(t) \approx t/\mathrm{Da}$ [7]. Substituting into Eq. (43) and solving the resulting equation, we obtain an approximation for the mass evolution for $t \geqslant \mathrm{Da}$,

$$M(t) \approx \left[M(\mathrm{Da})^{1-\beta} - \frac{2}{\sqrt{\beta}}\frac{1-\beta}{3-\beta}\left(\frac{2\pi}{\mathrm{Da}}\right)^{\frac{1-\beta}{2}}\left[t^{\frac{3-\beta}{2}} - \mathrm{Da}^{\frac{3-\beta}{2}}\right]\right]^{\frac{1}{1-\beta}}, \tag{50}$$

valid for $\beta \neq 1,3$. Recall that the case $\beta = 1$, corresponding to a first-order decay reaction, can be fully solved analytically. The case $\beta = 3$, which we do not analyze in detail here for brevity, behaves qualitatively similarly to $\beta > 3$, although extremely slow (logarithmic) decay of mass occurs at late times [7].

4.4 Reaction order $\beta < 1$ — Full-depletion regime

For $\beta < 1$, reaction rates increase with decreasing concentration, leading to full depletion in finite time. Under fully-mixed conditions, the depletion time t_f^B is given by Eq. (39). Recall that for

₅₂₉ sufficiently large Da full depletion occurs before transport must be taken into account. We thus focus
₅₃₀ on Damköhler numbers such that $\mathrm{Da} < t_f^B$.

₅₃₁ Under the combined effect of reaction and diffusion, mass is still fully depleted in a finite time t_f,
₅₃₂ different from t_f^B. Setting $M(t_f) = 0$ in Eq. (50) and solving for t_f yields [7]

$$t_f \approx \left[\mathrm{Da}^{\frac{3-\beta}{2}} + \frac{\sqrt{\beta}}{2} \frac{3-\beta}{1-\beta} \left(\frac{\mathrm{Da}}{2\pi} \right)^{\frac{1-\beta}{2}} \left[1 - (1-\beta)\,\mathrm{Da} \right] \right]^{\frac{2}{3-\beta}}. \tag{51}$$

₅₃₃ For sufficiently small detection limit c_m, we expect this prediction to provide a good estimate of the
₅₃₄ time at which the peak, mean concentration, and concentration variance reach zero. Interestingly,
₅₃₅ the depletion time decreases with decreasing Da. This decrease is due to the fact that, because in
₅₃₆ this regime reaction is faster at lower concentrations, stronger diffusion (smaller Da) leads to faster
₅₃₇ depletion when compared to a system with the same reaction rate. For this reason, both mass and
₅₃₈ peak concentration decay faster than the batch solution. In particular, for small $\mathrm{Da} \ll 1$, we find a
₅₃₉ simple power-law scaling with Da,

$$t_f \approx \left(\frac{\sqrt{\beta}}{2} \frac{3-\beta}{1-\beta} \right)^{\frac{2}{3-\beta}} \left(\frac{\mathrm{Da}}{2\pi} \right)^{\frac{1-\beta}{3-\beta}}. \tag{52}$$

₅₄₀ Note however that t_f/Da increases with decreasing Da, meaning that with increasing diffusion the
₅₄₁ depletion time occurs increasingly later than the time $t = \mathrm{Da}$ at which the Gaussian approximation
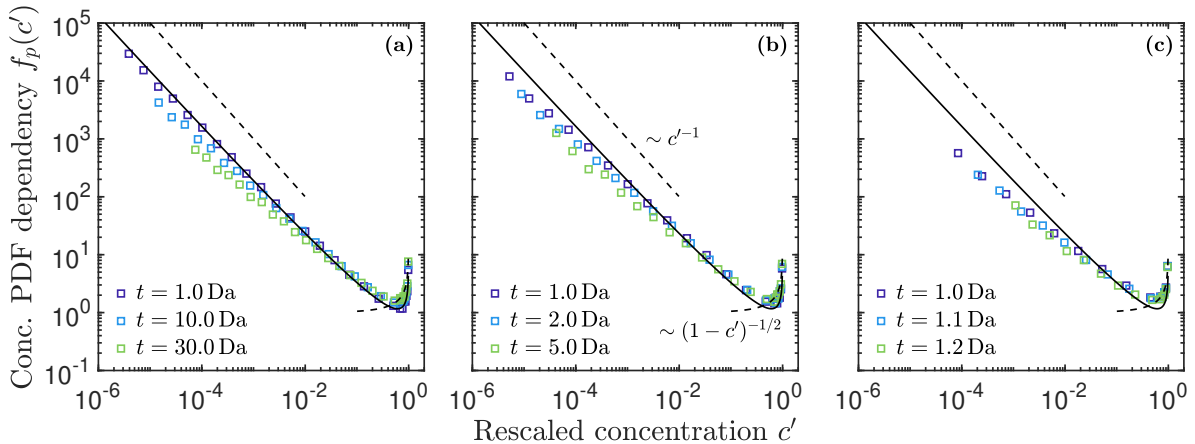₅₄₂ kicks in.

Figure 3: Functional dependency of the concentration PDF in terms of concentration rescaled by peak value, for $\beta = 1/2$ and **(a):** slow reaction, $\mathrm{Da} = 10^{-2}$, **(b):** intermediate reaction, $\mathrm{Da} = 10^{-1}$, and **(c):** fast reaction, $\mathrm{Da} = 1$. Colors stand for different times, with markers showing the results of resolved numerical simulations of the fully-coupled reaction–diffusion problem (35). Solid lines represent the analytical solution (47) under the weak-coupling model. The dashed lines show a pure $1/c'$ scaling for reference at low concentrations and the scaling of the inverse-square-root divergence near the maximum concentration value (see Eqs. (9) and (47)).

₅₄₃ To illustrate these results, we take $\beta = 1/2$ as a representative example. First, we compare the
₅₄₄ functional dependency of the concentration PDF (see Eqs. (46) and (47)) under the weak-coupling
₅₄₅ approximation to that obtained from resolved numerical simulations of Eq. (35) (see Appendix A
₅₄₆ and Appendix C). We focus on times t such that $\mathrm{Da} \leqslant t < t_f$ (see Eq. (51)). Results for different
₅₄₇ Damköhler numbers and times are shown in Fig. 3. Overall, the Gaussian approximation provides good
₅₄₈ estimates of the relative frequency of concentration values. Because, for $\beta < 1$, reaction is faster at
₅₄₉ lower concentrations, lower PDF values compared to the Gaussian prediction are observed at low values
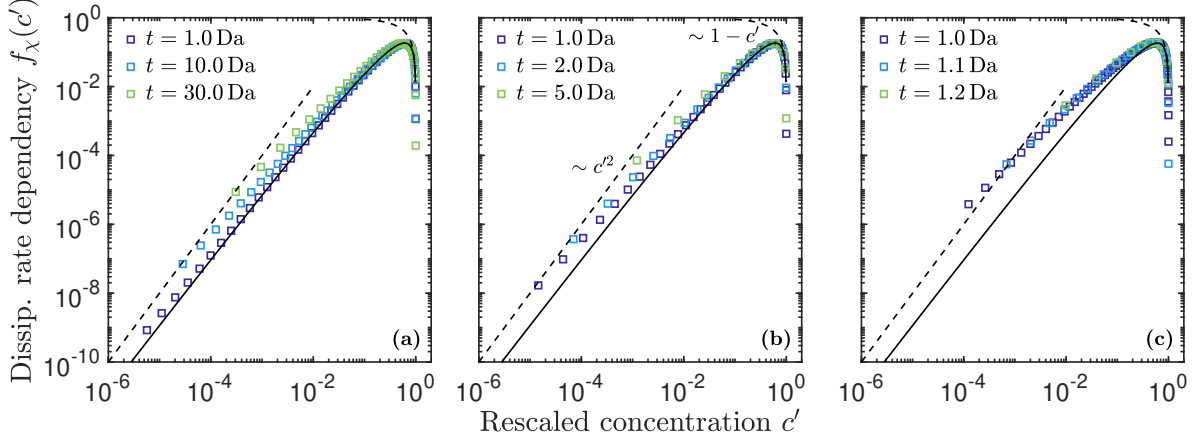
Figure 4: Functional dependency of the scalar dissipation rate in terms of concentration rescaled by peak value, for $\beta = 1/2$ and **(a):** slow reaction, $Da = 10^{-2}$, **(b):** intermediate reaction, $Da = 10^{-1}$, and **(c):** fast reaction, $Da = 1$. Colors stand for different times, with markers showing the results of resolved numerical simulations of the fully-coupled reaction–diffusion problem (35). Solid lines represent the analytical solution (49) under the weak-coupling model. The dashed lines show a pure c'^2 scaling for reference at low concentrations and the linear approach to zero near the peak concentration (see Eqs. (40) and (49)).

of concentration. This discrepancy at low concentrations also leads to a corresponding overprediction of higher concentrations, due to the normalization condition for the PDF. Although the bulk of the mass distribution is generally well captured, as discussed below, high Da leads to significant depletion at early times and results in a worse approximation.

Similar conclusions are reached from consideration of the functional dependency of the scalar dissipation rate (see Eqs. (48) and (49)), shown in Fig. 4. The Gaussian approximation again provides good estimates, but higher scalar dissipation rates, corresponding to higher gradients, are observed at low concentration values. The discrepancy is more pronounced in the same cases and for the same reasons as discussed regarding the concentration PDF, although in this case normalization does not play a role and thus no associated discrepancy at higher concentration values is observed.

Next, we turn to the evolution of the mass and peak concentration, shown in Fig. 5. As predicted by the weak-coupling approximation, both quantities reach zero in finite time as complete depletion occurs. However, due to the nonlinear nature of the reaction and the presence of diffusion, the peak dynamics differ from the total mass dynamics, as captured by Eqs. (45). Note the onset of a diffusive scaling of peak decay for low Damköhler, showing that the dynamics are controlled by diffusion at times $t \sim Da$ (corresponding to dimensional times on the order of the diffusion time). For late times, as concentration becomes smaller, reaction becomes more efficient. The dynamics depart from the diffusive scaling and full depletion eventually occurs. The slight underprediction of the depletion time t_f by the analytical approximation compared to the numerically-computed weak-coupling approximation results is due mostly to the breakdown of the linear variance growth approximation just before complete depletion, as observed in [7]. When comparing the predictions of the weak-coupling approximation to the resolved numerical simulations, we find overall good agreement. Regarding peak concentrations, the approximation of a sharp transition between batch and Gaussian-profile dynamics at $t = Da$ leads to some discrepancy at times $t \sim Da$, which becomes more pronounced with increasing Da. As the Damköhler number increases and the depletion time approaches Da from above ($t_f/Da \sim 1$, see Eq. (51)), stronger discrepancies are observed for both the mean concentration and the total mass, due to significant depletion before an approximately Gaussian profile is achieved. Nonetheless, the predictions for t_f still provide a reasonable approximation. Recall that, for higher $Da > t_f^B = 2$ (Eq. (39)), diffusion does not play a role before depletion the dynamics become well described by simple batch kinetics.
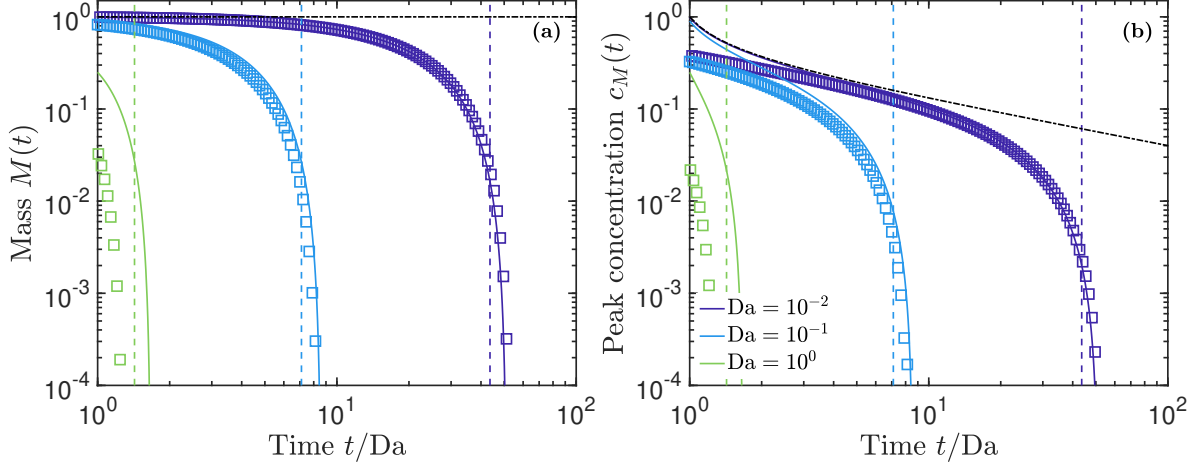
Figure 5: Temporal evolution of **(a):** total mass and **(b):** peak concentration for $\beta = 1/2$. Colors stand for different Damköhler numbers, markers show the results of resolved numerical simulations of the fully-coupled reaction–diffusion problem (35), solid lines are numerical results based on the weak-coupling model (Eqs. (45)), and dash-dotted lines show the purely-diffusive behavior. The vertical dashed lines show approximate analytical results for the depletion time (Eq. (51)).

Note that defining a mean concentration in terms of a fixed, reference spatial region, as done in [7], leads to a mean concentration scaling identical to that of the total mass, since in that case $\langle C(t)\rangle = M(t)/|\Omega|$ with constant domain size $|\Omega|$. Interestingly, when the mean concentration is instead defined, as here, in terms of the temporally-variable region where concentration is above a detection limit, the concentration mean and variance are instead fully controlled by the peak dynamics, see Eqs. (19) and (21). This leads also to a similar quality of the weak-coupling approximation when compared to the resolved simulations, as shown in Fig. 6. In particular, for low Damköhler numbers, our approach accurately predicts a transition from diffusion- to reaction-controlled dynamics, governed by the peak behavior described above, for both the mean concentration and the concentration variance.

4.5   Reaction order $1 < \beta < 3$ — Power-law-decay regime

In this regime, the interplay between reaction and diffusion leads to power-law mass decay at late times. Indeed, for $t \gg \mathrm{Da}$, Eq. (50) reduces to [7]

$$M(t) \approx \sqrt{\frac{2\pi}{\mathrm{Da}}} \left(\frac{\sqrt{\beta}}{2} \frac{3-\beta}{\beta-1} \right)^{\frac{1}{\beta-1}} t^{-\frac{3-\beta}{2(\beta-1)}}. \tag{53}$$

Substituting in Eq. (45b), and noting that, for $1 < \beta < 3$, as the peak concentration decreases the reactive term eventually dominates over the diffusive term, we have for late times

$$\frac{dc_M(t)}{dt} \approx -c_M^\beta(t). \tag{54}$$

Solving this equation, we obtain the late time peak decay

$$c_M(t) \approx [(\beta-1)t]^{-\frac{1}{\beta-1}}. \tag{55}$$

This behavior is characteristic of reaction-dominated conditions, and identical to the late-time batch dynamics, see Eq. (38). However, note that the total mass, Eq. (53), exhibits a different temporal scaling, as it results from the reactive decay of Gaussian-distributed concentration values undergoing diffusive spreading. This results, in contrast to the $\beta < 1$ regime, in slower asymptotic mass decay than predicted by batch dynamics, because in this case reaction is slower at lower concentrations.
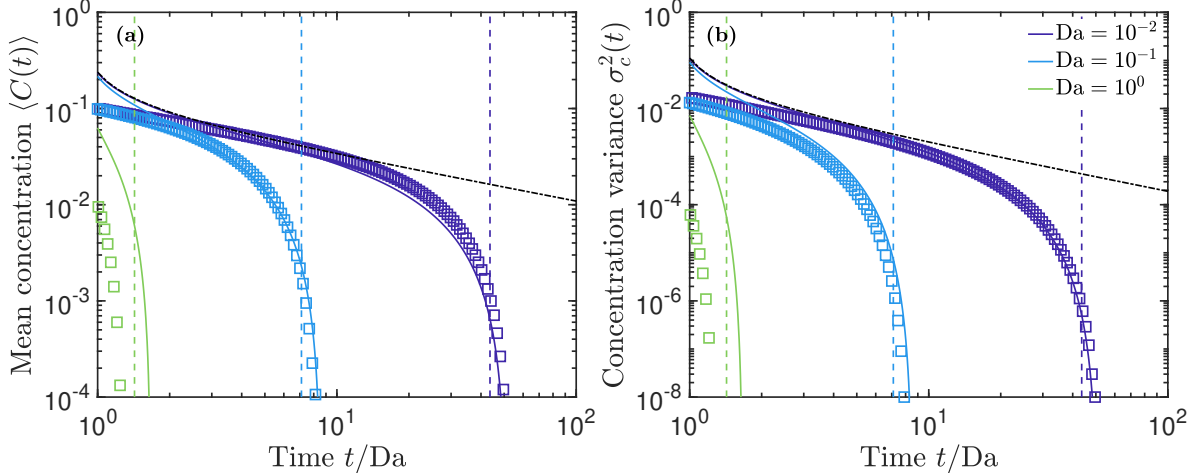
18

Figure 6: Temporal evolution of **(a):** mean concentration and **(b):** concentration variance for $\beta = 1/2$. Colors stand for different Damköhler numbers, markers show the results of resolved numerical simulations of the fully-coupled reaction–diffusion problem (35), solid lines are numerical results based on the weak-coupling model (Eqs. (45)), and dash-dotted lines show the purely-diffusive behavior. The vertical dashed lines show approximate analytical results for the depletion time (Eq. (51)).

We now take $\beta = 2$ as a representative example. Again, we start by assessing the performance of the Gaussian assumption for the functional dependency of the concentration PDF (Fig. 7). The approximation provides very good estimates of the frequency of occurrence of different concentrations. A slight underestimation of low concentrations, and corresponding overestimation of intermediate concentrations, occurs at late times for large Damköhler number. When considering the scalar dissipation rate (Fig. 8), we again observe very good agreement, with a corresponding slight but more discernible overestimation of concentration gradients at low concentrations. In this case, reaction is less efficient at low concentrations, so these results are somewhat counter-intuitive. Indeed, reaction is stronger and therefore has a more pronounced effect compared to diffusion at high concentrations. However, when the corresponding spatial profile is compared to a Gaussian of the same variance and maximum concentration, the latter underestimates the intermediate values but overestimates the tails. This is illustrated in Fig. 9 for the case of $\mathrm{Da} = 10^2$ at time $t = 10\,\mathrm{Da}$. This effect is slight, but it is more pronounced at the level of concentration gradients.

Next, we consider the evolution of total mass and peak concentration, see Fig. 10. The analytical approximation captures the asymptotic scalings correctly, although it slightly underpredicts the mass and overpredicts the peak concentration when compared to the numerically-computed weak-coupling approximation results. These discrepancies result in this case from small corrections to the $\sigma^2(t) \approx t/\mathrm{Da}$ diffusive spatial variance growth approximation of [7], implicit in Eq. (50) for the approximate late-time mass evolution. Again, the onset of a purely-diffusive scaling of peak decay is visible for low Damköhler before the asymptotic regime is reached. The weak-coupling approximation provides very good estimates of the resolved dynamics, even for $\mathrm{Da} \sim 1$. As expected, the largest discrepancies occur for times $t \sim \mathrm{Da}$, around which the approximation of a sharp transition between batch and Gaussian-profile dynamics has the most impact. In addition, a sharp depletion of mass can be observed at late times for the high-Da cases due to the detection limit. As expected, the transition from the dynamics predicted by the weak-coupling approximation to this sharp depletion occurs when the peak concentration becomes comparable to c_m.

As for the $\beta < 1$ case, the concentration mean and variance (Fig. 11) are controlled by the peak dynamics, see Eqs. (19) and (21). However, the changes in the size of the domain where concentration is larger than the detection limit lead to logarithmic corrections to the purely-reactive power-law scaling observed for the peak concentration. As for the mass and peak, the weak-coupling approximation
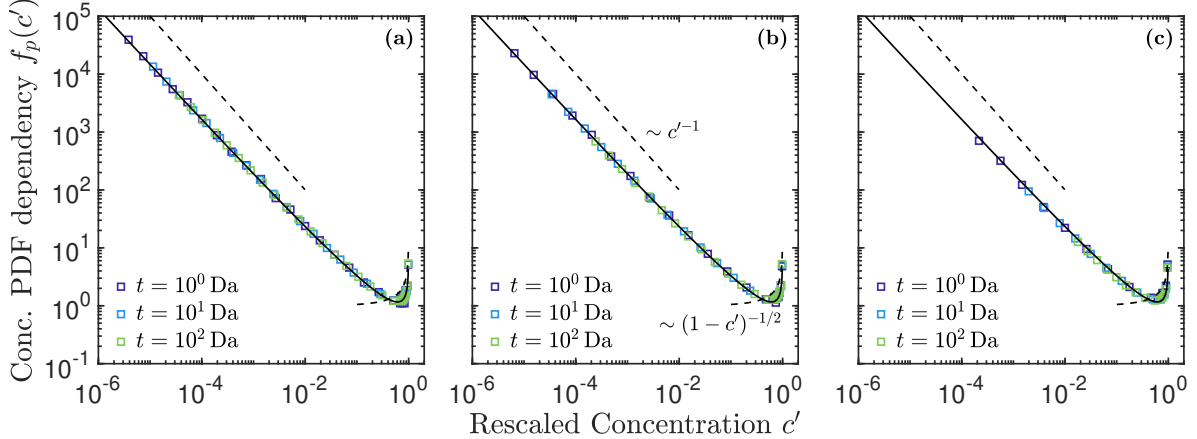
Figure 7: Functional dependency of the concentration PDF in terms of concentration rescaled by peak value, for $\beta = 2$ and **(a):** slow reaction, $\mathrm{Da} = 10^{-2}$, **(b):** intermediate reaction, $\mathrm{Da} = 1$, and **(c):** fast reaction, $\mathrm{Da} = 10^2$. Colors stand for different times, with markers showing the results of resolved numerical simulations of the fully-coupled reaction–diffusion problem (35). Solid lines represent the analytical solution (47) under the weak-coupling model. The dashed lines show a pure $1/c'$ scaling for reference at low concentrations and the scaling of the inverse-square-root divergence near the maximum concentration value (see Eqs. (9) and (47)).

provides very good predictions of the full dynamics, with the quality of the approximation improving for late times $t \gtrsim 10 \, \mathrm{Da}$. The discrepancies in the analytical *vs* numerical results for the weak-coupling approximation result from the discrepancies in the computation of the peak concentration discussed above.

4.6 Reaction order $\beta > 3$ — Incomplete-depletion regime

In this case, the substantial reaction slowdown associated with decreasing concentrations, enhanced by diffusion-induced dilution, prevents the complete depletion of mass by reaction, even for arbitrarily large times. Taking the limit $t \to \infty$ in Eq. (50) yields the leftover mass [7]

$$M_\infty \approx \left[1 + \left(1 + \frac{2}{(\beta - 3)\sqrt{(2\pi)^{\beta-1}\beta}} \right)(\beta - 1)\,\mathrm{Da} \right]^{-\frac{1}{\beta-1}}. \tag{56}$$

Substituting in Eq. (45b) as before, we now conclude that the late-time dominant contribution is diffusive, so that

$$\frac{dc_M(t)}{dt} \approx -\frac{\pi c_M^3(t)}{\mathrm{Da}\, M_\infty^2}. \tag{57}$$

Solving this equation leads, for large times, to

$$c_M(t) \approx M_\infty \sqrt{\frac{\mathrm{Da}}{2\pi t}}. \tag{58}$$

As the mass becomes constant at late times, the decay of peak concentration exhibits the signature of diffusive plume spreading. The mass in a well-mixed batch decreases asymptotically to zero, meaning the diffusing system leads to less efficient reaction, as expected since the reaction slows down strongly with decreasing concentration in this case. In contrast, however, the diffusion-governed peak decay is asymptotically faster than the corresponding batch prediction, Eq. (38).

To illustrate this regime, we take $\beta = 4$ as a representative example. As predicted by the weak-coupling approximation, reaction is sufficiently inefficient at low concentrations for diffusive spreading
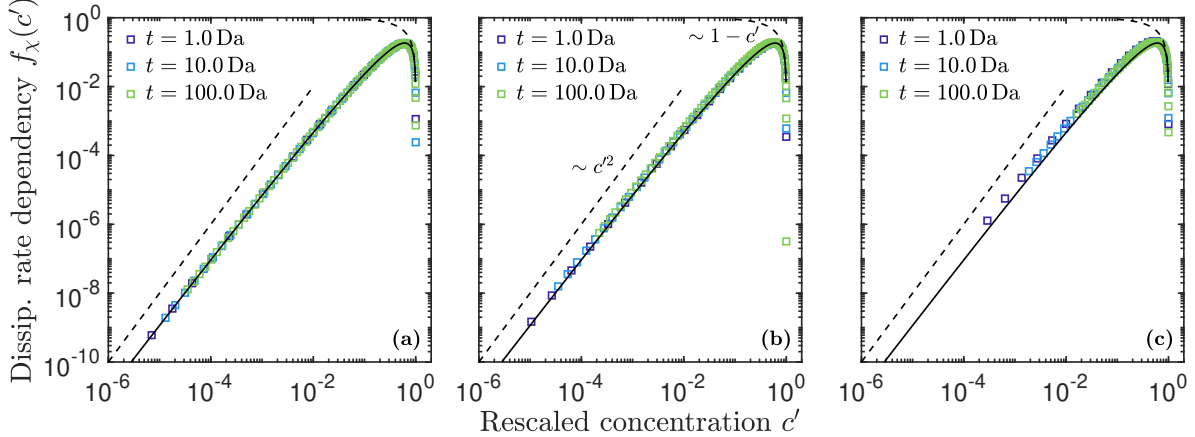
20

Figure 8: Functional dependency of the scalar dissipation rate in terms of concentration rescaled by peak value, for $\beta = 2$ and **(a):** slow reaction, $\mathrm{Da} = 10^{-2}$, **(b):** intermediate reaction, $\mathrm{Da} = 1$, and **(c):** fast reaction, $\mathrm{Da} = 10^2$. Colors stand for different times, with markers showing the results of resolved numerical simulations of the fully-coupled reaction–diffusion problem (35). Solid lines represent the analytical solution (49) under the weak-coupling model. The dashed lines show a pure c'^2 scaling for reference at low concentrations and the linear approach to zero near the peak concentration (see Eqs. (40) and (49)).

to completely arrest mass decay. This means that the system dynamics are essentially dominated by diffusion. Correspondingly, both the concentration PDF and the scalar dissipation rate show excellent agreement with the Gaussian prediction, as shown in Figs. 12 and 13, respectively.

Next, we consider the evolution of total mass and peak concentration, see Fig. 14. In this case, the analytical asymptotic predictions provide very accurate estimates of the weak-coupling dynamics. As expected from the analytical discussion, the results become indistinguishable from a purely diffusive system for sufficiently low Da. However, when comparing to the resolved numerical simulations, we find that the weak-coupling approximation underpredicts the asymptotic mass at higher Da. The main reason for the discrepancy is that, because the reaction is particularly inefficient at low concentrations, the system transitions to the Gaussian regime earlier in this case. Indeed, as shown by the dash-dotted lines in Fig. 14, assuming the transition occurs at $t = \mathrm{Da}/10$ rather than at $t = \mathrm{Da}$ leads to improved estimates of the asymptotic mass. To obtain this prediction, we proceed as for Eq. (56) but set the initial condition of the weak-coupling Gaussian regime at $t = \mathrm{Da}/10$ (see Eq. (42)), leading to

$$M_\infty \approx \left[1 + \left(1 + \frac{2 \cdot 10^{\frac{\beta-1}{2}}}{(\beta-3)\sqrt{(2\pi)^{\beta-1}\beta}} \right)(\beta-1)\frac{\mathrm{Da}}{10} \right]^{-\frac{1}{\beta-1}}. \qquad (59)$$

Note that the scaling of asymptotic mass with Da, and the relationship between asymptotic peak dynamics and asymptotic mass, Eq. (58), remain unchanged.

The concentration mean and variance for this case are shown in Fig. 15. The considerations pertaining to the $1 < \beta < 3$ case regarding the scaling of concentration mean and variance in terms of the peak concentration remain valid here, but in this case we observe logarithmically-corrected diffusive rather than reactive scalings. Once again, the low-Da case is indistinguishable from purely-diffusive dynamics. In addition, due to the low efficiency of reaction at low concentrations, the scaling behavior of both mean concentration and concentration variance remains purely diffusive, even for large Da. Overall, as for the total mass and peak concentration, the analytical approximation provides very good asymptotic estimates of the weak-coupling approximation, but better predictions of the fully-resolved dynamics are obtained by assuming the transition to the Gaussian regime occurs at time $t = \mathrm{Da}/10$ rather than at $t = \mathrm{Da}$.
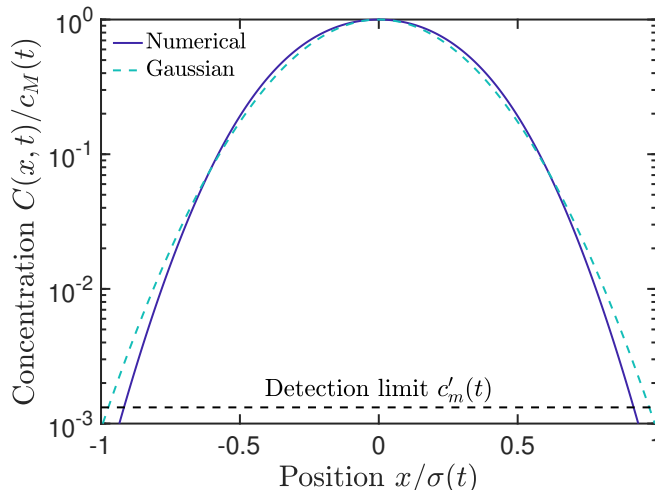
21

Figure 9: Concentration profile for $\beta = 2$ and $\mathrm{Da} = 10^2$, at time $t = 10\,\mathrm{Da}$. The solid line shows the profile computed from resolved numerical simulations of Eq. (35), and the dashed colored line shows a Gaussian profile with the same variance $\sigma^2(t)$ and maximum concentration $c_M(t)$. The horizontal dashed line shows the lower detection limit.

5   Discussion and conclusions

We have presented a detailed discussion of the theoretical and numerical properties of the concentration PDF of a reactive plume evolving under the coupled action of dilution and nonlinear reaction. The concentration PDF encodes the full point statistical variability of concentration values found throughout a spatial domain, and is therefore of central interest to both fundamental and applied reactive transport and risk assessment problems.

As a first step towards solving the full advection–diffusion–reaction system, we have conducted a detailed analysis of nonlinear decay of a single solute undergoing one-dimensional diffusion. We have shown that the weak-coupling approximation developed in [7] to quantify the evolution of total mass and mean concentration in a fixed reference domain can be extended to quantify the evolution of mean concentrations above a lower detection limit, along with the associated variability. In particular, we have found that the late-time Gaussian profile approximation leads to good predictions of the concentration PDF. Even for this simple one-dimensional diffusive system, the effective reaction kinetics governing these quantities exhibit rich dynamics. In contrast to well-mixed batch kinetics, the decay of concentrations at different Damköhler numbers can be dominated by diffusive or reactive effects at different times. Late-time concentrations can exhibit complete extinction, power-law decay, or complete arrest of reaction depending on the reaction order. The Gaussian approximation underlying the weak-coupling approach allows us to predict the associated concentration variance. Remarkably, the dynamics of the maximum concentration value, which provide the key control on the mean and variance of concentrations above a given detection threshold, differ qualitatively from the dynamics of total mass. In particular, for low Damköhler numbers, both the mean concentration and associated variability exhibit diffusion-controlled decay for times on the order of the diffusion time, for any reaction order. This diffusive control persists across all times and Damköhler numbers for strongly superlinear decay reactions (of order $\beta > 3$), whereas reaction is the fundamental mechanism controlling late-time and/or large-Da dynamics for lower reaction orders.

We have also derived a dynamical equation for the evolution of the concentration PDF in the nonlinear reaction–diffusion problem, showing that the impact of transport is encoded in the scalar dissipation rate seen as a function of concentration. It is important to note that the generalization of this equation to multiple dimensions, variable advection and/or diffusion tensor, and arbitrary reaction rates, for which concentration is no longer necessarily monotonically decreasing, is not straightforward.
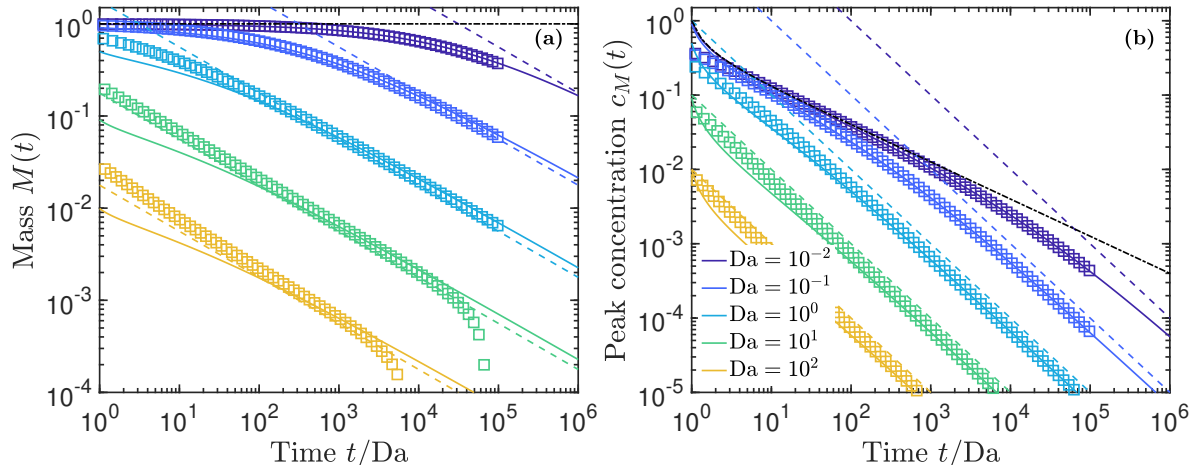
22

Figure 10: Temporal evolution of **(a):** total mass and **(b):** peak concentration for $\beta = 2$. Colors stand for different Damköhler numbers, markers show the results of resolved numerical simulations of the fully-coupled reaction–diffusion problem (35), solid lines are numerical results based on the weak-coupling model (Eqs. (45)), dashed lines show approximate asymptotic analytical results (Eqs. (53) and (55)), and dash-dotted lines show the purely-diffusive behavior.

Nonetheless, we believe the approach developed here, highlighting the role of the scalar dissipation rate, has the potential to form the basis for upscaling procedures in more complex systems. In particular, as discussed in Section 3, the dynamics of reaction under advection–diffusion in heterogeneous flows, in both two- and three-dimensional porous media, can be reduced to one-dimensional reaction–diffusion equations along the principal direction of compression on a collection of lamellar structures. With this in mind, further work will focus on the generalization of the approach developed here to the dynamics of Gaussian profiles subject to stretching-enhanced diffusion over an ensemble of lamellae.

Declarations

Conflicts of interest/Competing interests: The authors declare that they have no conflict of interest.
Availability of data and material: This work did not make use of or generate any datasets.
Code availability Numerical simulations used the `py-pde` open-source Python package for solving partial differential equations [79]. Please contact the authors for any additional information or requests.

A   Discretization

When computing the concentration PDF numerically, discretizations are typically employed both spatially and for the concentration values. As a simple example that highlights the central concepts, consider a regular spatial discretization into a grid with constant cell volume V_g, with each grid cell associated with the average concentration within it. According to the argument for constant concentration regions developed in the previous section, for each fixed time t, the concentration PDF is then
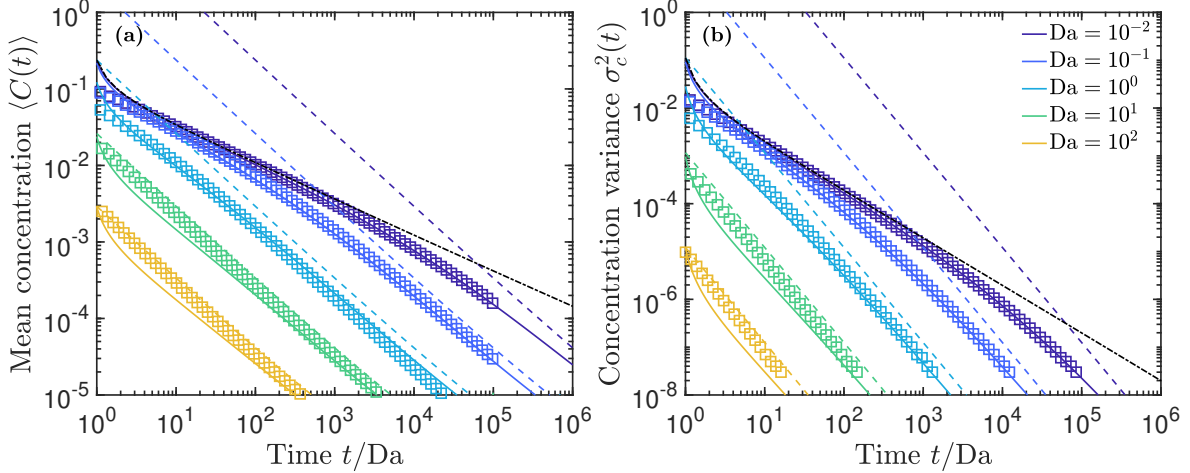
Figure 11: Temporal evolution of **(a):** mean concentration and **(b):** concentration variance for $\beta = 2$. Colors stand for different Damköhler numbers, markers show the results of resolved numerical simulations of the fully-coupled reaction–diffusion problem (35), solid lines are numerical results based on the weak-coupling model (Eqs. (45)), dashed lines show approximate asymptotic analytical results (Eqs. (19) and (21), using Eq. (55) for the peak concentration), and dash-dotted lines show the purely-diffusive behavior.

estimated as

$$p(c; t; N_g) = \frac{1}{N_g} \sum_{i=1}^{N_g} \delta[c - c_i(t)], \tag{60}$$

where $N_g = |\Omega|/V_g$ is the number of grid points and c_i is the average concentration in cell i. Note that the c_i associated with different cells are not necessarily all different.

Further discretizing concentration into bins leads to a probability mass function with values for the probability of concentration in each bin $B_k = [c^{(k)}, c^{(k+1)}[$, $k \geqslant 0$:

$$p_k(t; N_g) = \frac{1}{N_g} \sum_{i=1}^{N_g} H[c_i(t) - c^{(k)}] H[c^{(k+1)} - c_i(t)], \tag{61}$$

where $H(\cdot)$ is the Heaviside step function. This means that the probability of finding a concentration value in bin k is the fraction of cells where the concentration falls within bin k. If we take concentration bin widths Δc to be constant, $c^{(k)} = k\Delta c$ for $k \geqslant 0$, and approximate the PDF of concentration by dividing probabilities by Δc (as in Fig. 2), we obtain

$$p(c; t; N_g, \Delta c) = \frac{1}{N_g \Delta c} \sum_{i=1}^{N_g} H[c_i(t) - k\Delta c] H[(k+1)\Delta c - c_i(t)]. \tag{62}$$

These discretization procedures generalize directly to a multispecies system. In that case, concentration bins refer to the simultaneous attainment of concentration values of each species. The associated probabilities are computed as above by counting spatial cells where these values occur simultaneously. The procedure also generalizes directly to non-uniform and/or time-dependent spatial cell sizes and/or concentration bins. More involved techniques employing kernel reconstructions of the concentration field may be formalized in a similar manner [80–82].

The maximum resolution of the discretized concentration PDF described above is given by $1/(N_g \Delta c)$, and the maximum PDF value is $1/\Delta c$. We now discuss the impact of local spatial extrema, which can be associated with divergences of the continuous PDF as discussed in Section 2.3, on the discretized computation. It is also important to note that sources of error typically come into play in the
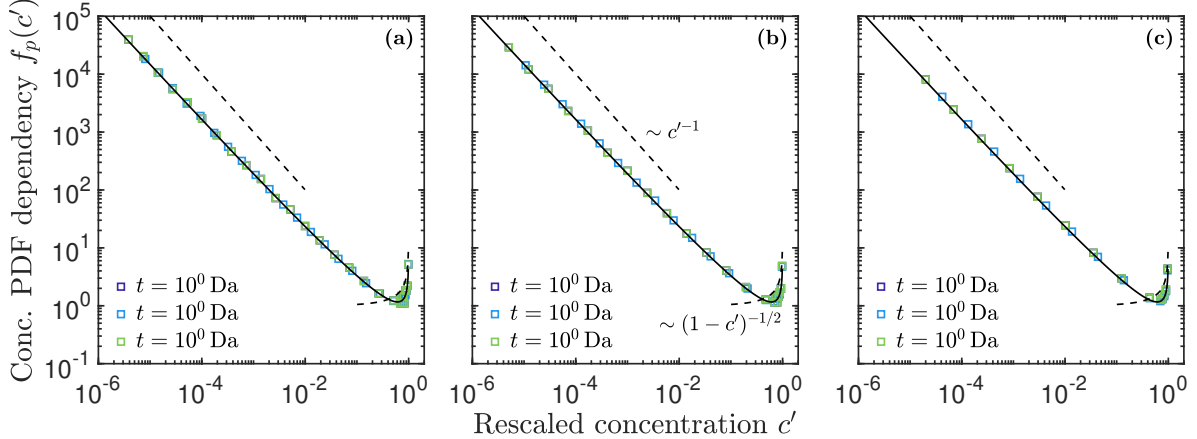
24

Figure 12: Functional dependency of the concentration PDF in terms of concentration rescaled by peak value, for $\beta = 2$ and **(a):** slow reaction, $\text{Da} = 10^{-2}$, **(b):** intermediate reaction, $\text{Da} = 1$, and **(c):** fast reaction, $\text{Da} = 10^2$. Colors stand for different times, with markers showing the results of resolved numerical simulations of the fully-coupled reaction–diffusion problem (35). Solid lines represent the analytical solution (47) under the weak-coupling model. The dashed lines show a pure $1/c'$ scaling for reference at low concentrations and the scaling of the inverse-square-root divergence near the maximum concentration value (see Eqs. (9) and (47)).

determination of the spatial concentration field. For example, if the latter is computed based on a particle tracking simulation of some transport and reaction dynamics, fluctuations arise due to the finite number of particles, whereas in a standard Eulerian simulation the spatial discretization impacts the determination of the true concentration field. We focus here on the error resulting from concentration discretization Δc, which is dominant given a sufficiently-resolved spatial concentration field.

Consider first a region of constant concentration. A delta peak $\delta(c-c_0)|\Omega_0|/|\Omega|$ in the concentration PDF, associated as discussed above to a subdomain Ω_0 of volume $|\Omega_0|$ where $C(\boldsymbol{x};t) = c_0$, corresponds under sufficiently fine spatial discretization to a discretized contribution $|\Omega_0|/(|\Omega|\Delta c)$. Thus, halving the concentration discretization Δc leads to a doubling of the numerically-computed peak. More generally, refining the discretization as $\Delta c \to a\Delta c$, $a < 1$, yields $p(c_0;t;N_g, a\Delta c) = ap(c_0;t;\Delta c)$. On the other hand, smooth extrema correspond to divergences only for spatial dimension $d = 1$, for which they lead to an inverse-square-root divergence, as shown in Section 2.3. In this case, averaging the concentration over a range Δc near the spatial extreme value c_0 yields $p(c_0;t;\Delta c) \propto 1/\sqrt{\Delta c}$, so that $p(c_0;t;a\Delta c) \approx \sqrt{a}p(c_0;t;\Delta c)$. Thus, observing these behaviors in a numerical computation is a signature of the presence of a spatial extremum, and the scaling behavior with concentration discretization refinement indicates its type.

B Dynamical equation for the concentration PDF

In this appendix, we provide a detailed derivation of the dynamical equation for the concentration PDF discussed in the main text, Eq. (34), by explicitly determining the diffusive transport and reaction contributions in Eq. (29). We first consider the effect of diffusion, $\Delta p_D(c;t)$. For one-dimensional diffusion and nonlinear concentration decay, assuming a symmetric initial condition about the origin and monotonically decreasing with distance from the latter, the spatial concentration profile retains these properties for all times. Therefore, we have $|\Lambda(c;t)| = 2$ for all concentrations within the range observed at time t, corresponding to the two points $x = \pm x_c(c;t)$ where $C(x;t) = c$. Furthermore, the concentration gradient magnitude is the same at $\pm x_c$, so that its harmonic average is simply $g_h(c;t) = \nabla C[-x_c(c;t),t] = -\nabla C[x_c(c;t),t]$. Using Eq. (8) and the fact that $|\Lambda(c;t)|$ is time-independent within
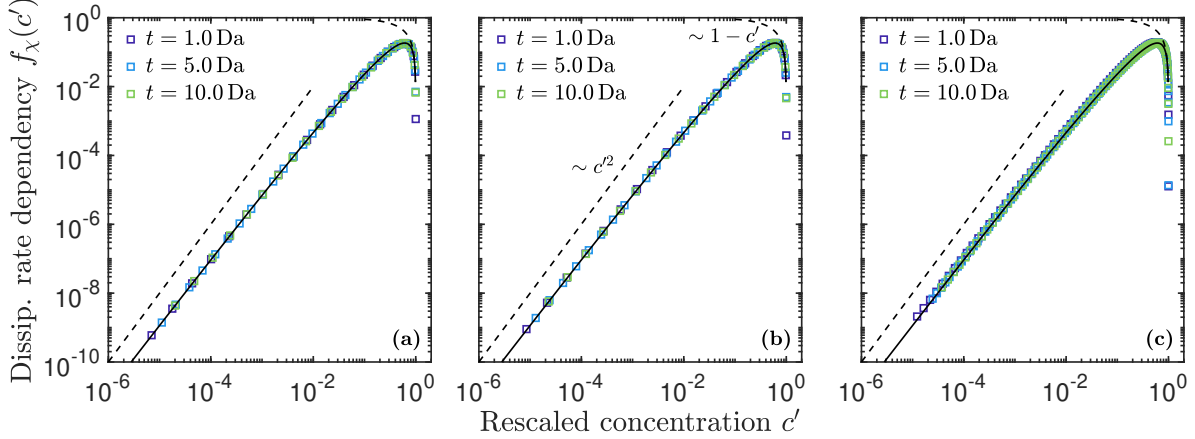
Figure 13: Functional dependency of the scalar dissipation rate in terms of concentration rescaled by peak value, for $\beta = 2$ and **(a):** slow reaction, $\mathrm{Da} = 10^{-2}$, **(b):** intermediate reaction, $\mathrm{Da} = 1$, and **(c):** fast reaction, $\mathrm{Da} = 10^2$. Colors stand for different times, with markers showing the results of resolved numerical simulations of the fully-coupled reaction–diffusion problem (35). Solid lines represent the analytical solution (49) under the weak-coupling model. The dashed lines show a pure c'^2 scaling for reference at low concentrations and the linear approach to zero near the peak concentration (see Eqs. (40) and (49)).

the concentration range observed, we can write the change in the concentration PDF as

$$\frac{\partial p(c;t)}{\partial t} = -p(c;t)\left[\frac{\partial \ln |\Omega(t)|}{\partial t} + \frac{\partial \ln g_h(c;t)}{\partial t}\right].\tag{63}$$

If a fixed reference volume is considered, the term corresponding to the change of $|\Omega(t)|$ in time is zero. As discussed in the main text, we focus here on the case of a minimum detection limit c_m and a time-varying domain $\Omega(t)$ where $c > c_m$.

In order to compute the terms in square brackets, we consider the time evolution of quantities on a given concentration surface (in one dimension, at the points $\pm x_c(c;t)$). By definition, the change in time of concentration over such a surface is zero, so that

$$\frac{\partial C[x_c(c;t);t]}{\partial t} = \left[\frac{\partial x_c(c;t)}{\partial t}\frac{\partial C(x;t)}{\partial x} + \frac{\partial C(x;t)}{\partial t}\right]_{x=x_c(c;t)} = 0\tag{64}$$

Taking into account that, at $x = x_c$, $\partial/\partial x = -g_h(c;t)\partial/\partial c$, the changes associated with transport lead to

$$\frac{\partial x_c(c;t)}{\partial t} = \frac{1}{2g_h(c;t)}\frac{\partial \chi(c;t)}{\partial c},\tag{65}$$

where $\chi(c;t) = \chi_x[\pm x_c(c;t);t] = Dg_h^2(c;t)$ is the concentration-dependent scalar dissipation rate. The same approach for the variation of the concentration gradient leads to

$$\frac{\partial g_h(c;t)}{\partial t} = -\left[\frac{\partial x_c(c;t)}{\partial t}\frac{\partial^2 C(x;t)}{\partial x^2} + \frac{\partial}{\partial t}\frac{\partial C(x;t)}{\partial x}\right]_{x=x_c(c;t)},\tag{66}$$

and we find

$$\frac{\partial \ln g_h(c;t)}{\partial t} = \frac{1}{2}\frac{\partial^2 \chi(c;t)}{\partial c^2} - \frac{1}{4}\frac{\partial \ln \chi(c;t)}{\partial c}\frac{\partial \chi(c;t)}{\partial c}.\tag{67}$$

The change in domain volume $\Omega(t) = 2x_c(c_m;t)$ due to dilution of concentration below the detection limit c_m obeys

$$\frac{\partial |\Omega(t)|}{\partial t} = 2\frac{\partial x_c(c_m;t)}{\partial t},\tag{68}$$
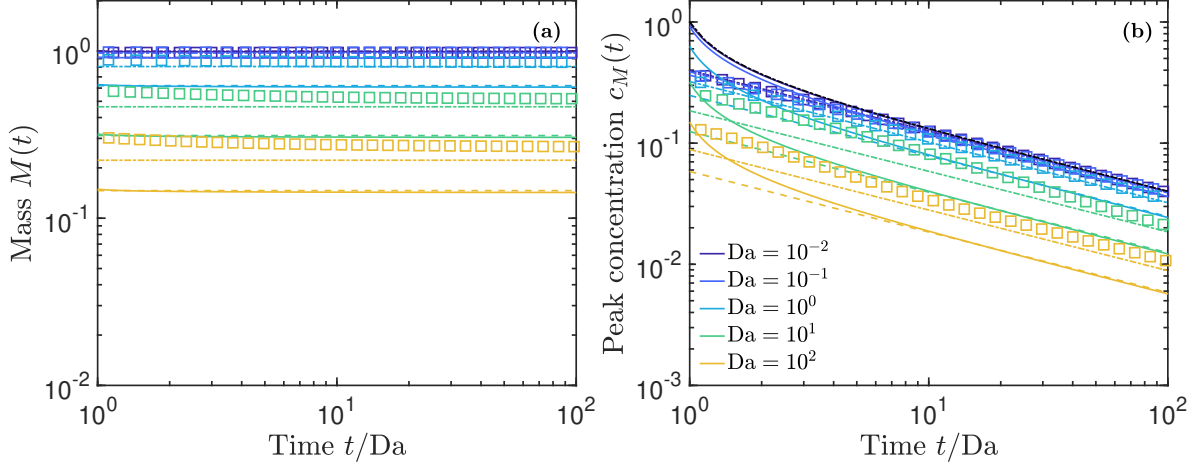
26

Figure 14: Temporal evolution of **(a):** total mass and **(b):** peak concentration for $\beta = 4$. Colors stand for different Damköhler numbers, markers show the results of resolved numerical simulations of the fully-coupled reaction–diffusion problem (35), solid lines are numerical results based on the weak-coupling model (Eqs. (45)), and dashed lines show approximate asymptotic analytical results (Eqs. (56) and (58)). Dash-dotted lines show analytical results assuming the transition to the Gaussian regime occurs at time $t = \mathrm{Da}/10$ rather than at $t = \mathrm{Da}$ (Eq. (59)).

Using Eq. (65), this leads to

$$\frac{\partial |\Omega(t)|}{\partial t} = \frac{1}{g_h(c_m; t)} \left.\frac{\partial \chi(c; t)}{\partial c}\right|_{c=c_m}, \tag{69}$$

so that, dividing through by $|\Omega(t)|$ and using Eq. (8),

$$\frac{\partial \ln |\Omega(t)|}{\partial t} = \frac{p(c_m; t)}{2} \left.\frac{\partial \chi(c; t)}{\partial c}\right|_{c=c_m}. \tag{70}$$

Using Eq. (63) for the transport contribution, these results lead to

$$\Delta p_D(c; t) = p(c; t) \left[\frac{1}{4}\frac{\partial \ln \chi(c; t)}{\partial c}\frac{\partial \chi(c; t)}{\partial c} - \frac{1}{2}\frac{\partial^2 \chi(c; t)}{\partial c^2} - \frac{p(c_m; t)}{2}\left.\frac{\partial \chi(c; t)}{\partial c}\right|_{c=c_m}\right]. \tag{71}$$

We now turn to the reaction term, Δp_R. Consider a small change dc in the concentrations due to reaction only, over a small time interval dt. The probability $p(c; t + dt)\, dc$ of finding concentrations in the infinitesimal vicinity dc of c decreases due to reaction at rate $r(c)$ away from c, and increases due to decrease in nearby concentrations towards c. Thus,

$$[p(c; t + dt) - p(c; t)]\, dc = \sum_{j=1}^{n_s}[r(c + dc)p(c + dc; t) - r(c)p(c; t)]\, dt. \tag{72}$$

Expanding the first term on each side in Taylor series, and dividing through by dt and dc, we obtain

$$\frac{\partial p(c; t)}{\partial t} = \frac{\partial r(c)p(c; t)}{\partial c}. \tag{73}$$

When a fixed minimum concentration detection limit is considered, as discussed above, it is necessary to take the change in volume (in one dimension, length) $|\Omega(t)|$ due to reactive decay of the minimum
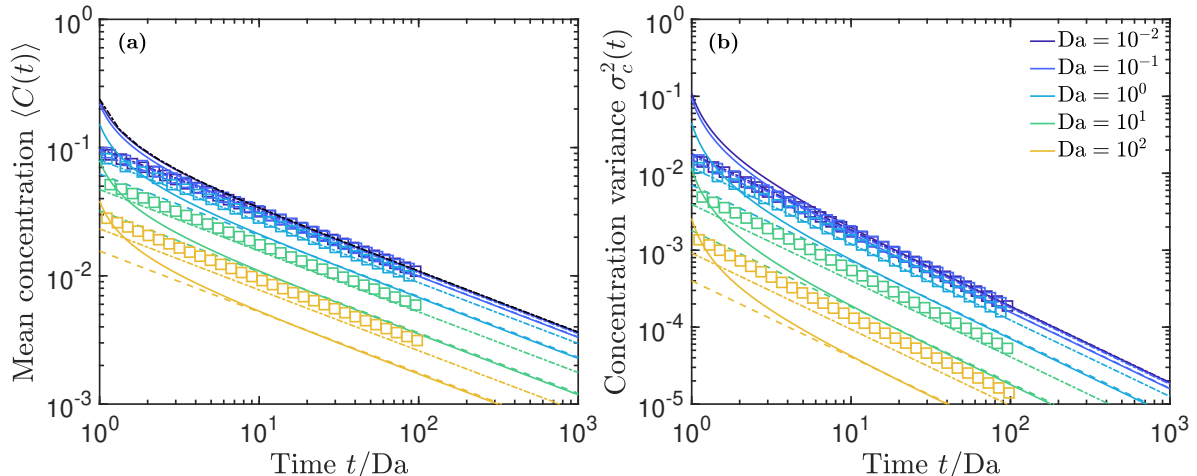
27

Figure 15: Temporal evolution of **(a):** mean concentration and **(b):** concentration variance for $\beta = 4$. Colors stand for different Damköhler numbers, markers show the results of resolved numerical simulations of the fully-coupled reaction–diffusion problem (35), solid lines are numerical results based on the weak-coupling model (Eqs. (45)), and dashed lines show approximate asymptotic analytical results (Eqs. (19) and (21), using Eqs. (56) and (58) for the peak concentration). Dash-dotted lines show analytical results assuming the transition to the Gaussian regime occurs at time $t = \mathrm{Da}\,/10$ rather than at $t = \mathrm{Da}$ (Eqs. (19) and (21), using Eqs. (58) and (59) for the peak concentration).

concentration into account. Using the same techniques as before, we obtain for the change in the domain size due to reaction:

$$\frac{\partial \ln |\Omega(t)|}{\partial t} = -p(c_m; t) r(c_m). \tag{74}$$

Thus, the complete effect of reaction is

$$\Delta p_R(c; t) = \frac{\partial r(c) p(c; t)}{\partial c} + p(c; t) p(c_m; t) r(c_m). \tag{75}$$

Note that integration of the right-hand side from $c = c_m$ to $c = \infty$ yields zero, which ensures the reactive contribution conserves probability for arbitrary $r(c)$. Substituting the effects of transport and reaction, Eqs. (33) and (33), in Eq. (29) leads to the dynamical Eq. (34) for the evolution of the concentration PDF under one-dimensional diffusion and nonlinear decay.

C   Numerical methods

In this appendix, we provide details on the numerical methods used to integrate the weak-coupling equations (45) and the reaction–diffusion equation (35). Regarding Eqs. (45), which are ordinary differential equations, we implemented a standard fourth-order Runge–Kutta method in the C++ language. This method was chosen for its simplicity of implementation and high accuracy, and also because, as an explicit method, it provides a convenient approach to integrate these nonlinear equations without requiring numerical root-finding methods. We employed a time step $\Delta t = 10^{-2} \min\{\mathrm{Da}, 1/\mathrm{Da}\}$ for the temporal discretization, which we verified led to consistently converged results.

For the fully-coupled reaction–diffusion problem, Eq. (35), we employed the `py-pde` open-source Python package for solving partial differential equations [79]. We used a regular finite difference discretization of a one-dimensional domain of half-width L and second-order centered differences for the spatial derivative approximations. For the time integration, we employed an explicit Forward Euler scheme. We set reflecting boundary conditions at the edges of the computational domain, but we verified that the latter was sufficiently large that no appreciable mass reached the edges, rendering

28

Table 1: Discretization parameters used in computing solutions of Eq. (35) to determine the mass and concentration peak, mean, and variance. For these computations, we employed a temporal discretization $\Delta t = a \min\{\mathrm{Da}, 1/\mathrm{Da}\}$ and a spatial discretization $\Delta x = b\sqrt{\Delta t/\mathrm{Da}}$. The corresponding values of (a, b) for different reaction orders β and Damköhler numbers Da are given in the table.

$\beta \setminus \mathrm{Da}$	10^{-2}	10^{-1}	10^{0}	10^{1}	10^{2}
1/2	$(10^{-4}, 1)$	$(10^{-4}, 1)$	$(5 \cdot 10^{-7}, 1)$	$-$	$-$
2	$(10^{-2}, 1)$	$(10^{-2}, 1)$	$(10^{-2}, 1)$	$(10^{-1}, 2)$	$(10, 4)$
4	$(10^{-3}, 1)$	$(10^{-2}, 1)$	$(10^{-2}, 1)$	$(10^{-1}, 1)$	$(10^{-1}, 1)$

Table 2: Discretization parameters used in computing solutions of Eq. (35) to determine the concentration PDF and scalar dissipation rate. For these computations, we employed a temporal discretization $\Delta t = a \min\{\mathrm{Da}, 1/\mathrm{Da}\}$ and a spatial discretization $\Delta x = \sqrt{\Delta t/\mathrm{Da}}$. The corresponding values of a for different reaction orders β and Damköhler numbers Da are given in the table.

$\beta \setminus \mathrm{Da}$	10^{-2}	10^{-1}	10^{0}	10^{1}	10^{2}
1/2	10^{-4}	10^{-4}	$5 \cdot 10^{-6}$	$-$	$-$
2	10^{-3}	$-$	10^{-4}	$-$	10^{-2}
4	10^{-4}	$-$	10^{-4}	$-$	10^{-1}

the choice of boundary conditions irrelevant. Since the late-time variance growth is approximately diffusive, $L = 10\sqrt{t_m/\mathrm{Da}}$, where t_m is the maximum simulation time, may be used as a simple estimate of necessary domain size. However, because of the lower detection limit $c_m = 10^{-6}$ used in the computation of the quantities of interest, we found that in practice it was never necessary to use $L > 1500$ for the simulations conducted here. We note that, for $\beta < 1$, where complete depletion of concentrations can happen in finite time, the increase of reaction rates with decreasing concentration values can lead to numerical issues, because very low concentrations can drop below zero within a time step. We avoid this issue by setting negative concentrations to zero before computing reaction rates. We chose the spatial and temporal discretizations so as to ensure good accuracy while maintaining reasonable simulation times. The discretization parameters for different system parameters β and Da are summarized in Table 1 for the mass and concentration peak, mean, and variance calculations, and in Table 2 for the concentration PDF and scalar dissipation rate.

The concentration PDF was obtained by counting discretized spatial locations where the concentration value fell within prescribed bins (see also Section A). In order to accurately resolve both low and high concentrations, we employed n_ℓ logarithmically-spaced concentration bins for concentrations between the lower detection limit c_m and $2c_M(t)/3$, where the time-dependent peak value $c_M(t)$ was determined from the numerical concentration profiles, and n_h linearly-space bins for the remaining concentrations between $2c_M(t)/3$ and $c_M(t)$. For the lower, intermediate, and higher time examined in each case, we employed $(n_\ell, n_h) = (20, 10)$, $(15, 8)$, and $(10, 6)$, respectively. The scalar dissipation rate was calculated according to Eq. (77b) by numerically computing the spatial derivative at each discretized spatial location (in the rising limb of the symmetric concentration profile), using second-order central differences. The corresponding concentration values at each spatial location were recorded and used to obtain the scalar dissipation rate as a function of concentration.

D Problem setup and nondimensionalization

This appendix provides additional details on the nondimensionalization used in Section 4. Denoting nondimensionalized quantities by an asterisk, we have

$$C_*(x_*; t_*) = \frac{C(s_0 x_*, \tau_R t_*)}{c_0}, \qquad\qquad r_*(c_*) = \frac{\tau_R}{c_0} r(c_0 c_*) = c_*^{\beta}, \qquad (76)$$

where the characteristic reaction time $\tau_R = \kappa^{-1} c_0^{1-\beta}$. The minimum and maximum concentrations $c_M(t)$ and $c_m(t)$ are normalized in the same manner. Similarly, the nondimensional spatial variance $\sigma_*^2(t_*) = \sigma^2(\tau_R t_*)/s_0^2$. The concentration PDF and scalar dissipation are then nondimensionalized accordingly as

$$p_*(c_*; t_*) = c_0 p(c_0 c_*; \tau_R t_*), \tag{77a}$$

$$\chi_*(c_*; t_*) = \frac{\tau_R}{c_0^2} \chi(c_0 c_*; \tau_R t_*) = \frac{1}{2\,\mathrm{Da}} \left(\frac{\partial C_*(x_*, t_*)}{\partial x_*} \right)^2_{x_* = x_c(c)/s_0}, \tag{77b}$$

with the Damköhler number $\mathrm{Da} = \tau_D/\tau_R$.

Note that, in nondimensional units, the pulse initial condition is given by a unit-width rectangle centered at the origin,

$$C_*(x_*; 0) = H\left(1/2 - x_*\right) H\left(1/2 + x_*\right), \tag{78}$$

which implies $p_*(c_*; 0) = \delta(c_* - 1)$. The batch concentration $c_B(t)$ for the well-mixed problem is nondimensionalized as above, and $c_{B*}(0) = 1$.

E Batch dynamics

Here, we provide some details on the equations governing the well-mixed batch problem discussed in Section 4 and its relation to the concentration PDF. Noting that $p(c; t) = \delta[c - c_B(t)]$ for the batch problem, where $c_B(t) = C(x; t)$ is the homogeneous concentration over the domain, and assuming $c_B(t) > c_m$, Eq. (34) becomes

$$\frac{\partial p(c; t)}{\partial t} = \frac{\partial r(c) p(c; t)}{\partial c}. \tag{79}$$

Multiplying through by c and integrating over c (using integration by parts on the right hand side), we recover the standard well-mixed rate law for the batch concentration as a function of time,

$$\frac{dc_B(t)}{dt} = -r[c_B(t)]. \tag{80}$$

Substituting Eq. (76) for the rate yields Eq. (37).

Once $c_B(t)$ drops below c_m, at some time t_m, the domain $\Omega(t)$ where concentrations are above this detection limit becomes empty, and the concentration PDF becomes ill-defined. By convention, we can set $c_B(t > t_m) = 0$ and $p(c; t > t_m) = \delta(c)$, which conveys the meaning that concentrations are zero everywhere (below the detection limit).

References

[1] Carl I Steefel, Donald J DePaolo, and Peter C Lichtner. Reactive transport modeling: An essential tool and a new research approach for the earth sciences. *Earth Planet. Sci. Lett*, 240(3-4):539–558, 2005.

[2] Laura Guadagnini, Alessandra Menafoglio, X Sanchez-Vila, and Alberto Guadagnini. Probabilistic assessment of spatial heterogeneity of natural background concentrations in large-scale groundwater bodies through functional geostatistics. *Sci. Total Environ.*, 740:140139, 2020.

[3] Erica R Siirila and Reed M Maxwell. Evaluating effective reaction rates of kinetically driven solutes in large-scale, statistically anisotropic media: Human health risk implications. *Water Resour. Res.*, 48(4), 2012.

[4] Ilenia Battiato, Daniel M Tartakovsky, Alexandre M Tartakovsky, and T Scheibe. On breakdown of macroscopic models of mixing-controlled heterogeneous reactions in porous media. *Adv. Water Resour.*, 32(11):1664–1673, 2009.

[5] I Battiato and DM Tartakovsky. Applicability regimes for macroscopic models of reactive transport in porous media. *J. Contam. Hydrol.*, 120:18–26, 2011.

[6] A. Hubert, T. Aquino, H. Tabuteau, Y. Méheust, and T. Le Borgne. Enhanced and non-monotonic effective kinetics of solute pulses under michaelis–menten reactions. *Adv. Water Resour.*, 146: 103739, 2020.

[7] Charlotte Le Traon, Tomás Aquino, Camille Bouchez, Kate Maher, and Tanguy Le Borgne. Effective kinetics driven by dynamic concentration gradients under coupled transport and reaction. *Geochim. Cosmochim. Acta*, 306:189–209, 2021. ISSN 0016-7037. doi: https://doi.org/10.1016/j. gca.2021.04.033.

[8] EE O'brien. The probability density function (pdf) approach to reacting turbulent flows. In *Turbulent reacting flows*, pages 185–218. Springer, 1980.

[9] Stephen B Pope. Pdf methods for turbulent reactive flows. *Prog. Energy Combust. Sci.*, 11(2): 119–192, 1985.

[10] Stephen B Pope. Lagrangian pdf methods for turbulent flows. *Annu. Rev. Fluid Mech.*, 26(1): 23–63, 1994.

[11] PR Van Slooten, Jayesh, and SB Pope. Advances in pdf modeling for inhomogeneous turbulent flows. *Phys. Fluids*, 10(1):246–265, 1998.

[12] Steven R Hanna. The exponential probability density function and concentration fluctuations in smoke plumes. *Bound.-Layer Meteorol.*, 29(4):361–375, 1984.

[13] Eugene Yee. The shape of the probability density function of short-term concentration fluctuations of plumes in the atmospheric boundary layer. *Bound.-Layer Meteorol.*, 51(3):269–298, 1990.

[14] Eugene Yee and R Chan. A simple model for the probability density function of concentration fluctuations in atmospheric plumes. *Atmos. Environ.*, 31(7):991–1002, 1997.

[15] Jean-Rémi Alisse and Claude Sidi. Experimental probability density functions of small-scale fluctuations in the stably stratified atmosphere. *J. Fluid Mech.*, 402:137–162, 2000.

[16] RJ Munro, PC Chatwin, and N Mole. The high concentration tails of the probability density function of a dispersing scalar in the atmosphere. *Bound.-Layer Meteorol.*, 98(2):315–339, 2001.

[17] József Bakosi, Pasquale Franzese, and Zafer Boybeyi. Probability density function modeling of scalar mixing from concentrated sources in turbulent channel flow. *Phys. Fluids*, 19(11):115106, 2007.

[18] César Dopazo and Edward E O'Brien. An approach to the autoignition of a turbulent mixture. *Acta Astronaut.*, 1(9-10):1239–1266, 1974.

[19] P. Givi, J. I. Ramos, and W. A. Sirignano. Probability density function calculations in turbulent chemically reacting round jets, mixing layers and one-dimensional reactors. *J. Non-Equilib. Thermodyn.*, 10(2):75–104, 1985.

[20] MS Anand and SB Pope. Calculations of premixed turbulent flames by pdf methods. *Combust. Flame*, 67(2):127–142, 1987.

[21] Rodney O Fox. Computation of turbulent reactive flows: first-principles macro/micromixing models using probability density function methods. *Chem. Eng. Sci.*, 47(9-11):2853–2858, 1992.

[22] Daniel Connell Haworth. Progress in probability density function methods for turbulent reacting flows. *Prog. Energy Combust. Sci.*, 36(2):168–259, 2010.

[23] S Broyda, Marco Dentz, and DM Tartakovsky. Probability density functions for advective–reactive transport in radial flow. *Stoch. Environ. Res. Risk. Assess.*, 24(7):985–992, 2010.

[24] Vivek Kapoor and Peter K Kitanidis. Concentration fluctuations and dilution in aquifers. *Water Resour. Res.*, 34(5):1181–1193, 1998.

[25] Aldo Fiori and Gedeon Dagan. Concentration fluctuations in transport by groundwater: Comparison between theory and field experiments. *Water Resour. Res.*, 35(1):105–112, 1999.

[26] Aldo Fiori and Gedeon Dagan. Concentration fluctuations in aquifer transport: A rigorous first-order solution and applications. *J. Contam. Hydrol.*, 45(1-2):139–163, 2000.

[27] Mark Shvidler and Kenzi Karasaki. Probability density functions for solute transport in random field. *Transp. Porous Media*, 50(3):243–266, 2003.

[28] M. Dentz, D. Bolster, and T. Le Borgne. Concentration statistics for transport in random media. *Phys. Rev. E*, 80:010101(R), 2009.

[29] Marco Dentz and Daniel M Tartakovsky. Probability density functions for passive scalars dispersed in random velocity fields. *Geophys. Res. Lett.*, 37(24), 2010.

[30] Tanguy Le Borgne, Marco Dentz, and Emmanuel Villermaux. The lamellar description of mixing in porous media. *J. Fluid Mech.*, 770:458–498, 2015.

[31] Emmanuel Villermaux. Mixing versus stirring. *Annu. Rev. Fluid Mech.*, 51:245–273, 2019.

[32] Matteo Icardi and Marco Dentz. Probability density function (pdf) models for particle transport in porous media. *GEM - Int. J. Geomath.*, 11(1):1–17, 2020.

[33] Mayumi Hamada, Luis Cueto-Felgueroso, and Pietro de Anna. Diffusion limited mixing in confined media. *Phys. Rev. Fluids*, 5(12):124502, 2020.

[34] Olaf A Cirpka, Ronnie L Schwede, Jian Luo, and Marco Dentz. Concentration statistics for mixing-controlled reactive transport in random heterogeneous media. *J. of Contam. Hydrol.*, 98 (1-2):61–74, 2008.

[35] Xavier Sánchez-Vila, Alberto Guadagnini, and Daniel Fernàndez-Garcia. Conditional probability density functions of concentrations for mixing-controlled reactive transport in heterogeneous aquifers. *Mathematical geosciences*, 41(3):323–351, 2009.

[36] Pietro De Anna, Tanguy Le Borgne, Marco Dentz, Diogo Bolster, and Philippe Davy. Anomalous kinetics in diffusion limited reactions linked to non-Gaussian concentration probability distribution function. *J. Chem. Phys.*, 135(17):174104, 2011.

[37] A. Bellin, G. Severino, and A. Fiori. On the local concentration probability density function of solutes reacting upon mixing. *Water Resour. Res.*, 47(1), 2011.

[38] Olaf A Cirpka, Felipe PJ de Barros, Gabriele Chiogna, and Wolfgang Nowak. Probability density function of steady state concentration in two-dimensional heterogeneous porous media. *Water Resour. Res.*, 47(11), 2011.

[39] Gabriele Chiogna and Alberto Bellin. Analytical solution for reactive solute transport considering incomplete mixing within a reference elementary volume. *Water Resour. Res.*, 49(5):2589–2600, 2013.

[40] Nicolae Suciu, Florin A Radu, Sabine Attinger, L Schüler, and Peter Knabner. A fokker–planck approach for probability distributions of species concentrations transported in heterogeneous media. *J. Comput. Appl. Math.*, 289:241–252, 2015.

[41] Nicole Sund, Tomás Aquino, and Diogo Bolster. Effective models for transport in complex heterogeneous hydrologic systems. In Patricia Maurice, editor, *Encyclopedia of Water: Science, Technology, and Society*. John Wiley & Sons, 2019. ISBN 9781119300762.

[42] Peter C Lichtner and DM Tartakovsky. Stochastic analysis of effective rate constant for heterogeneous reactions. *Stoch. Env. Res. Risk. A.*, 17(6):419–429, 2003.

[43] D. M. Tartakovsky, M. Dentz, and P. C. Lichtner. Probability density functions for advective-reactive transport with uncertain reaction rates. *Water Resour. Res.*, 45(7), 2009.

[44] Daniel M Tartakovsky and Svetlana Broyda. Pdf equations for advective–reactive transport in heterogeneous porous media with uncertain properties. *J. Contam. Hydrol.*, 120:129–140, 2011.

[45] Daniele Venturi, Daniel M Tartakovsky, Alexandre M Tartakovsky, and George E Karniadakis. Exact pdf equations and closure approximations for advective-reactive transport. *J. Comput. Phys.*, 243:323–343, 2013.

[46] T. Le Borgne, P. D. Huck, M. Dentz, and E. Villermaux. Scalar gradients in stirred mixtures and the deconstruction of random fields. *J. Fluid Mech.*, 812:578–610, 2017. doi: 10.1017/jfm.2016.799.

[47] Emilie Guilbert, Christophe Almarcha, and Emmanuel Villermaux. Chemical reaction for mixing studies. *Phys. Rev. Fluids*, 6(11):114501, 2021.

[48] Pietro De Anna, Marco Dentz, Alexandre Tartakovsky, and Tanguy Le Borgne. The filamentary structure of mixing fronts and its control on reaction kinetics in porous media flows. *Geophys. Res. Lett.*, 41(13):4586–4593, 2014.

[49] Tanguy Le Borgne, Timothy R Ginn, and Marco Dentz. Impact of fluid deformation on mixing-induced chemical reactions in heterogeneous flows. *Geophys. Res. Lett.*, 41(22):7898–7906, 2014.

[50] Joaquín Jiménez-Martínez, Pietro de Anna, Hervé Tabuteau, Régis Turuban, Tanguy Le Borgne, and Yves Méheust. Pore-scale mechanisms for the enhancement of mixing in unsaturated porous media and implications for chemical reactions. *Geophys. Res. Lett.*, 42(13):5316–5324, 2015.

[51] Aditya Bandopadhyay, Tanguy Le Borgne, Yves Méheust, and Marco Dentz. Enhanced reaction kinetics and reactive mixing scale dynamics in mixing fronts under shear flow for arbitrary damköhler numbers. *Adv. Water Resour.*, 100:78–95, 2017.

[52] YB Zeldovich. The asymptotic law of heat transfer at small velocities in the finite domain problem. *Zh. Eksp. Teoret. Fiz*, 7(12):1466–1468, 1937.

[53] Julio M Ottino and JM Ottino. *The kinematics of mixing: stretching, chaos, and transport*, volume 3. Cambridge university press, 1989.

[54] Tanguy Le Borgne, Marco Dentz, Diogo Bolster, Jesus Carrera, Jean-Raynald De Dreuzy, and Philippe Davy. Non-Fickian mixing: Temporal evolution of the scalar dissipation rate in heterogeneous porous media. *Adv. Water Resour.*, 33(12):1468–1475, 2010.

[55] Felipe PJ De Barros, Marco Dentz, Jonas Koch, and Wolfgang Nowak. Flow topology and scalar mixing in spatially heterogeneous flow fields. *Geophys. Res. Lett.*, 39(8), 2012.

[56] Nicholas B Engdahl, Timothy R Ginn, and Graham E Fogg. Scalar dissipation rates in non-conservative transport systems. *J. Contam. Hydrol.*, 149:46–60, 2013.

[57] Deepashree S Raje and Vivek Kapoor. Experimental study of bimolecular reaction kinetics in porous media. *Environ. Sci. Technol.*, 34(7):1234–1239, 2000.

[58] Carolyn M Gramling, Charles F Harvey, and Lucy C Meigs. Reactive transport in porous media: A comparison of model prediction with laboratory visualization. *Environ. Sci. Technol.*, 36(11): 2508–2514, 2002.

[59] FJ Valdes-Parada and J Alvarez-Ramirez. On the effective diffusivity under chemical reaction in porous media. *Chem. Eng. Sci.*, 65(13):4100–4104, 2010.

[60] FJ Valdés-Parada, CG Aguilar-Madera, and J Alvarez-Ramirez. On diffusion, dispersion and reaction in porous media. *Chem. Eng. Sci.*, 66(10):2177–2190, 2011.

[61] JMC Pereira, JEP Navalho, ACG Amador, and JCF Pereira. Multi-scale modeling of diffusion and reaction–diffusion phenomena in catalytic porous layers: comparison with the 1d approach. *Chem. Eng. Sci.*, 117:364–375, 2014.

[62] William E Ranz. Applications of a stretch model to mixing, diffusion, and reaction in laminar and turbulent flows. *AIChE J.*, 25(1):41–47, 1979.

[63] Tomás Aquino and Tanguy Le Borgne. The diffusing-velocity random walk: a spatial-Markov formulation of heterogeneous advection and diffusion. *J. Fluid Mech.*, 910:A12, 2021.

[64] Willliam Feller. *An introduction to probability theory and its applications*, volume 2. John Wiley & Sons, 2008.

[65] Lars Hörmander. *The analysis of linear partial differential operators I: Distribution theory and Fourier analysis.* Springer, 2015.

[66] Frank E Marble and James E Broadwell. The coherent flame model for turbulent chemical reactions. Technical Report TRW-9-PU, Project SQUID, Purdue Univ., West Lafayette, IN, 1977.

[67] Emmanuel Villermaux. Mixing by porous media. *C. R. Mécanique*, 340(11-12):933–943, 2012.

[68] Tanguy Le Borgne, Marco Dentz, and Emmanuel Villermaux. Stretching, coalescence, and mixing in porous media. *Phys. Rev. Lett.*, 110(20):204501, 2013.

[69] George Keith Batchelor. The effect of homogeneous turbulence on material lines and surfaces. *Proc. R. Soc. A*, 213(1114):349–366, 1952.

[70] R Betchov. An inequality concerning the production of vorticity in isotropic turbulence. *J. Fluid Mech.*, 1(5):497–504, 1956.

[71] WJ Cocke. Turbulent hydrodynamic line stretching: consequences of isotropy. *Phys. Fluids*, 12 (12):2488–2492, 1969.

[72] Wm T Ashurst, AR Kerstein, RM Kerr, and CH Gibson. Alignment of vorticity and scalar gradient with strain rate in simulated navier–stokes turbulence. *Phys. Fluids*, 30(8):2343–2353, 1987.

[73] SS Girimaji and SB Pope. Material-element deformation in isotropic turbulence. *J. Fluid Mech.*, 220:427–458, 1990.

[74] D Martínez-Ruiz, P Meunier, B Favier, L Duchemin, and E Villermaux. The diffusive sheet method for scalar mixing. *J. Fluid Mech.*, 837:230–257, 2018.

[75] Patrice Meunier and Emmanuel Villermaux. The diffusive strip method for scalar mixing in two dimensions. *J. Fluid Mech.*, 662:134–172, 2010.

[76] J. Heyman, D. R. Lester, R. Turuban, Y. Méheust, and T. Le Borgne. Stretching and folding sustain microscale chemical gradients in porous media. *Proc. Natl. Acad. Sci. U.S.A.*, 2020.

[77] Jerôme Duplat and Emmanuel Villermaux. Mixing by random stirring in confined mixtures. *J. Fluid Mech.*, 617:51–86, 2008.

[78] Daniel R Lester, Marco Dentz, and Tanguy Le Borgne. Chaotic mixing in three-dimensional porous media. *J. Fluid Mech.*, 803:144–174, 2016.

[79] David Zwicker. py-pde: A python package for solving partial differential equations. *J. Open Source Softw.*, 5(48):2158, 2020. doi: 10.21105/joss.02158. URL https://doi.org/10.21105/joss.02158.

[80] Vlad I Morariu, Balaji Vasan Srinivasan, Vikas C Raykar, Ramani Duraiswami, and Larry S Davis. Automatic online tuning for fast gaussian summation. In *Advances in Neural Information Processing Systems*, volume 21, pages 1113–1120, Vancouver, 2008. Citeseer.

[81] Daniel Fernàndez-Garcia and Xavier Sánchez-Vila. Optimal reconstruction of concentrations, gradients and reaction rates from particle distributions. *J. Contam. Hydrol.*, 120:99–114, 2011.

[82] Guillem Sole-Mari, Diogo Bolster, Daniel Fernàndez-Garcia, and Xavier Sanchez-Vila. Particle density estimation with grid-projected and boundary-corrected adaptive kernels. *Adv. Water Resour.*, 131:103382, 2019.